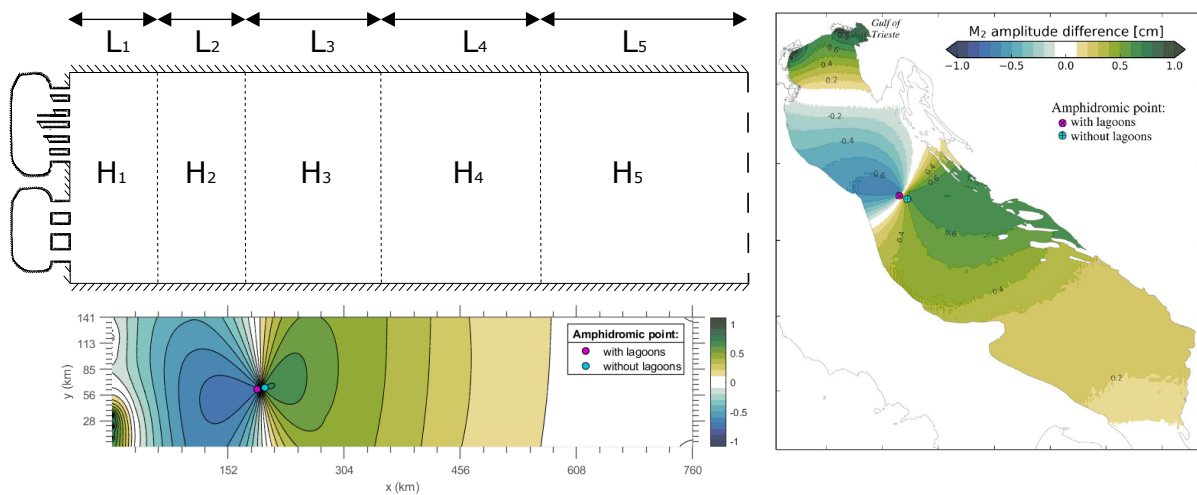


The influence of lagoons on large-scale tidal dynamics: an idealized modelling study

Faculty of Engineering Technology

Civil Engineering and Management

K. M. Hermann
Master Thesis, January 2020



The influence of lagoons on large-scale tidal dynamics: an idealized modelling study

Kai M. Hermann

In partial fulfilment of the requirements for the degree of Master of Science in Water Engineering and Management at the University of Twente

January 2020

Enschede

Contact K.M.Hermann@alumnus.utwente.nl

Graduation committee	Dr. ir. P. C. Roos	University of Twente
	Dr. ir. G. H. P. Campmans	University of Twente
	Dr. H. M. Schuttelaars	Delft University of Technology

Pictures on the cover page: (left) Geometry and M_2 tidal range difference between idealized model simulations with lagoons and without lagoons and (right) the tidal range difference computed by a complex model (Ferrarin et al., 2017)

Abstract

Complex numerical modelling studies of the Adriatic Sea suggest that tidal inlet systems such as the Venice lagoon have a significant impact on the tidal dynamics, affecting the entire Adriatic Sea. However, the underlying physical mechanisms are not yet understood. We present an idealized modelling study to investigate the tidal interaction between lagoons and an adjacent sea. To model the tidal interaction between a lagoon and a sea, a classical Taylor model is combined with a Helmholtz basin at the closed end. We studied the influence of so-called sub-critical lagoons (with an eigenfrequency above the forcing tidal frequency) and super-critical lagoons (with an eigenfrequency below the forcing tidal frequency) on the tidal dynamics of the sea with a parameter sensitivity analysis. The physical mechanism induced by a lagoon, affecting the large-scale tidal dynamics of the sea, involves a radiating wave originating from the lagoon. This radiating wave causes a phase-shift of the reflected Kelvin wave, resulting in an along-basin shift of the amphidromic system. Additionally, enhanced energy dissipation due to bottom friction in the inlet channels of the lagoon leads to a cross-basin shift of the amphidromic point. Finally, we tested our model by comparing a simulation of the Adriatic Sea with the results of the above-mentioned complex model. Effects of the tidal interaction between the lagoons and the Adriatic Sea of the idealized model showed good agreement with the results of the aforementioned complex model. The results confirmed that lagoons affect the tidal dynamics of the entire Adriatic Sea. Additionally, we showed that the simulated shift in the amphidromic point in the Adriatic Sea occurs due to the sub-critical nature of the lagoons. Our results indicate that — as the proximity to resonance of the lagoon governs the response in the adjacent sea — altering the geometry of the lagoons (e.g. through dredging operations) may cause back-effects in the adjacent sea.

Contents

1	Introduction	4
1.1	Background	4
1.2	Knowledge gap	5
1.3	Objective and research questions	6
1.4	Methods	6
1.4.1	Develop an idealized model (RQ1)	6
1.4.2	Study the tidal interaction between a lagoon and the sea (RQ2)	6
1.4.3	Apply the model to the Adriatic Sea and compare the results with complex model simulations (RQ3)	7
1.5	Report outline	7
2	Model	8
2.1	Model formulation	8
2.2	Solution method	10
2.3	Procedure to determine the bottom friction coefficient	11
3	Results	13
3.1	Interaction lagoon and adjacent sea	14
3.1.1	Along-basin shifts of amphidromic point	14
3.1.2	Cross-basin shifts of the amphidromic point	17
3.2	Application to the Adriatic Sea and comparison with complex model simulations	18
4	Discussion	21
4.1	Along-basin shift of the amphidromic point	21
4.2	Cross-basin shift of the amphidromic point	21
4.3	Influence of geometry and boundary conditions on the model results	22
4.4	Comparison between the idealized model and the complex model	22
5	Conclusion and outlook	24
	Appendices	28
A	Deriving the model equations of the sea basin	28
A.1	Linearisation of shallow water equations	28
A.2	Klein-Gordon equation and the Polarisation equation	29
A.3	Dispersion relation and wavenumber	30
B	Solving the coefficients of the system	31
C	Transformation from the basic model to the Adriatic Sea model	34
C.1	Basic model	35
C.2	Step 1: Multiple compartments in the sea basin	36
C.3	Step 2: Multiple inlet channels in the lagoon	37
C.4	Step 3: Multiple lagoons	38
C.5	Step 4: Dirichlet boundary condition as open boundary	39

1 Introduction

1.1 Background

Tidal dynamics affect the general tidal propagation, tidal currents and sediment transport and therefore play a crucial role in ecology, navigation and coastal safety. Numerous modelling studies have been carried out to investigate the implications of tidal dynamics for the changing coastal environment. Recently, the influence of tidal inlet systems on tidal dynamics has been put in a new perspective. Modelling studies of the Adriatic Sea show that lagoons affect the tidal dynamics of the entire Adriatic Sea. As about 10% of the world’s coastline consists of tidal inlet systems such as lagoons (Glaeser, 1978), understanding their effect on the tidal dynamics is an important part of coastal management.

To gain a better understanding of tidal dynamics, *process-based models* are often used. Process-based models give a mathematical representation of one or several processes within a certain domain, based on the physical mechanisms governing these processes. We distinguish two types of process-based models in this study: *complex models* and *idealized models*. A complex model is used to reproduce a natural system as completely as possible, including all processes that could significantly affect the quantitative accuracy of the model, using high resolutions for a detailed geometry (Murray, 2003). Idealized models make use of a simplified geometry and simplified description of physics. As a result, idealized models have relatively low computational demands and thus allow for an extensive parameter sensitivity analysis (Kumar et al., 2015). Both complex models and idealized models have been used to study the tidal dynamics of the Adriatic Sea.

A complex, high resolution 3D finite element model of the Adriatic Sea, that included the Marano-Grado, Venice- and Po-Delta lagoons unravelled the significant influence of lagoons on large-scale tidal dynamics (Ferrarin et al., 2017). This they did by computing the tidal range — the maximum free surface elevation of the water surface on a specific geographical location — and the position of the amphidromic point. An amphidromic point is a geographical location which has zero tidal range for one harmonic constituent of the tide, meaning the tidal wave rotates around this point. Figure 1 illustrates that the inclusion of lagoons in the complex model of the Adriatic Sea affects the M_2 tidal dynamics of the whole Adriatic Sea, causing tidal range differences and a shift in the amphidromic point. These results highlight the relevance of lagoons, as the effects of modifications in the lagoon are not limited to the tidal dynamics inside the lagoon, but may extend far in the open sea.

While such complex models present the significance of the effect of lagoons on the tidal dynamics, the underlying physical mechanism is more difficult to analyse due to high computational demands. Idealized modelling studies, on the other hand, are specifically designed to study a physical mechanism in more detail through exploratory models. Taylor (1922) introduced an idealized modelling approach for semi-enclosed, rectangular-shaped tidal basins with uniform depth. This approach proved suitable to compute the gross patterns of tidal dynamics for basins such as the Irish Sea, and later also the Gulf of California or the Adriatic Sea (Hendershott & Speranza, 1971). The solution of the Taylor problem can be written as a superposition of analytical wave solutions: an incoming Kelvin wave, a reflected Kelvin wave and an infinite number of Poincaré modes, that are generated at the closed end of the model. Brown (1973) introduced a *collocation* method, to obtain the coefficients of the Poincaré modes. Rienecker & Teubner (1980) extended Taylor’s model by including linear bottom friction in the model. Frictional effects lead to dissipation of wave energy, damping the amplitude of the waves, causing a shift in the amphidromic points towards the reflected wave. Roos & Schuttelaars (2009) extended the model further by taking horizontally viscous effects — illustrating the diffusion of momentum and dissipation of energy — into account. Finally, to reproduce a more realistic topography and study its influence on tide propagation and amplification, Roos & Schuttelaars (2011) added topographic steps to the model to account for depth variations. The idealized model results were compared to observations, and despite simplified geometry and topography, the model obtained good agreement with observations in the Gulf of California, the Persian Gulf and the Adriatic Sea.

While Taylor’s approach presents a suitable idealized modelling approach for semi-enclosed basins such as the Adriatic Sea, a so-called *Helmholtz basin* (Miles & Munk, 1961) presents a convenient method to model the tidal dynamics of smaller systems such as lagoons. A Helmholtz basin has a spatially uniform free surface elevation connected to the sea through an inlet channel with uniform depth

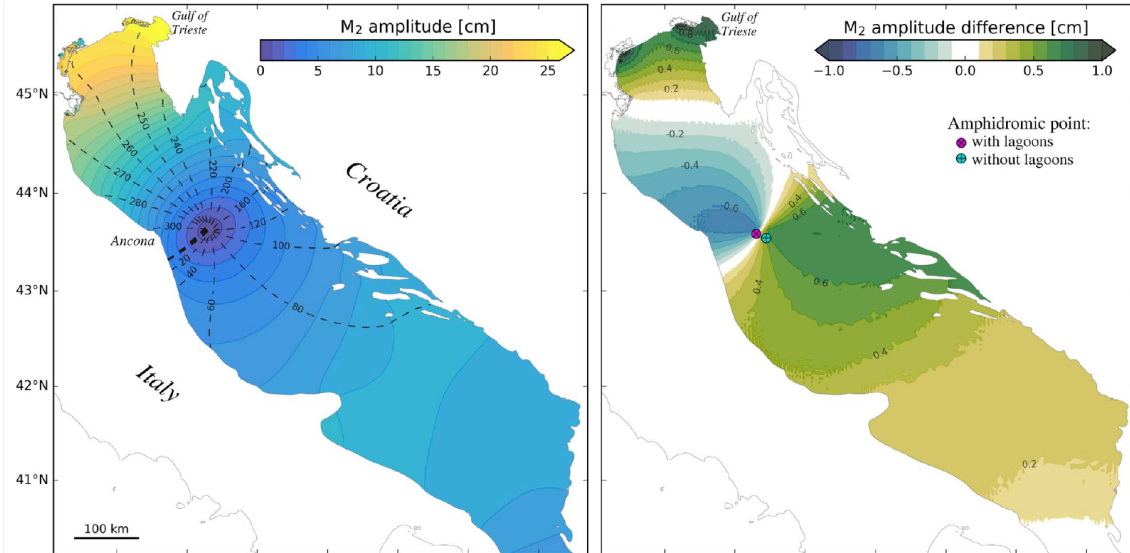


Figure 1: Model results of Ferrarin et al. (2017) for (left) the M_2 tidal range and phase computed from the simulation with the lagoons, and (right) the tidal range difference between the scenario with and without lagoons. Dashed lines (left) denote the co-phase lines. Differences between numerical simulations are computed as the results of the simulation that includes lagoons minus the reference simulation without lagoons.

and width. Herman (2007) compared the tidal hydrodynamics of a Helmholtz basin with a complex 3D model and found that the Helmholtz basin gives an accurate representation of the overall volume transport and water exchange with the adjacent sea. The volume transport through the inlet channel is essential to capture the effect of *radiation damping* (Roos & Schuttelaars, 2015), which plays a crucial role in the tidal interaction between a lagoon and the sea. Radiation damping occurs when the tidal oscillations within the Helmholtz basin trigger co-oscillations in the adjacent sea. These co-oscillations form waves radiating back into the sea. Numerous studies showed that radiation damping significantly affects the tidal dynamics (e.g Miles, 1971; Garrett, 1975; Maas, 1997; Brouwer et al., 2013). Thus, a Helmholtz basin neglects spatial variation in the lagoon and the inlet channels and provides an accurate representation of the water exchange with the adjacent sea, capturing the effect of radiation damping.

The concept of resonance — which implies strong amplification of the elevation amplitude inside the basin with respect to its value at sea when the frequency of the periodic forcing at sea approximates the eigenfrequency of the basin — has an important role in the dynamics of a Helmholtz basin. In a Helmholtz basin, either a tide is amplified as when the basin is near resonance, or it is suppressed, far away from resonance (Maas, 1997). However, damping mechanisms, such as radiative damping and energy dissipation due to bottom friction, significantly affect this amplification or suppression. Roos & Schuttelaars (2015) investigated the effects of a channel with multiple Helmholtz basins' (termed tidal retention basins), co-oscillating with an adjacent sea. They found that the response in the sea depends on whether the basin is *sub-critical* or *super-critical*. These states are characterized by the ratio between the forcing frequency of the tide (σ) and the *frictionless* eigenfrequency (σ_0) of the system, with $\sigma/\sigma_0 < 1$ for a so-called *sub-critical* basin, and $\sigma/\sigma_0 > 1$ for a *super-critical* basin.

1.2 Knowledge gap

Modelling studies of the Adriatic Sea have shown us that lagoons have a significant impact on the tidal dynamics of the entire Adriatic Sea (Ferrarin et al., 2017). However, the underlying physical mechanisms are not yet understood as it is currently unknown how lagoons affect the large-scale tidal dynamics in an adjacent sea, such as the Adriatic Sea.

1.3 Objective and research questions

This research aims to solve the research gap presented in 1.2. To do this, the following research objective is defined:

“To explain how lagoons affect the large-scale tidal dynamics in an adjacent sea, such as the Adriatic Sea.”

To support this objective, we seek to answer the following research questions:

RQ1. *How can we develop an idealized model to investigate the tidal interaction between a lagoon and an adjacent sea?*

RQ2. *How do lagoons affect the large-scale tidal dynamics of an adjacent sea?*

RQ3. *Can we simulate the effects of lagoons in the Adriatic Sea while maintaining our idealized modelling approach and how does this compare to results from the existing modelling study by Ferrarin et al. (2017)?*

1.4 Methods

This section presents the methods used to answer the research questions presented in section 1.3. It starts with a description of the idealized modelling approach (RQ1). Next, we describe the systematic approach to study the tidal interaction between a lagoon and the sea (RQ2). The last section presents how we test our model with an application to the Adriatic Sea (RQ3).

1.4.1 Develop an idealized model (RQ1)

In order to reproduce the tidal interaction between the sea and a lagoon, we combined Taylor’s approach with a Helmholtz basin. We required a model with low computational demands, such that it allowed for an extensive parameter sensitivity analysis which was needed to answer the second research question. First, we extended Taylor’s approach to account for frictional effects and depth variations, similar to the approach of Roos & Schuttelaars (2011). Next, Helmholtz basins were included in the model to account for the presence of lagoons. The Helmholtz basins were modelled as such, that we could easily vary the amount, the locations and the dimensions.

1.4.2 Study the tidal interaction between a lagoon and the sea (RQ2)

To investigate the model results, we performed simulations for a semi-diurnal lunar M_2 tidal constituent for a sea basin with uniform width and depth, forced through a Riemann boundary condition at the open boundary of the system. A Helmholtz basin was placed at the centre of the closed boundary (figure 3a). The dimensions of the Helmholtz basin and the sea basin are chosen to roughly represent the geometry of the Venice lagoon and the Adriatic Sea, respectively. We varied the surface area of the lagoon for a number of simulations to investigate the influence of the lagoon on the large-scale tidal dynamics. Altering the surface area changed the frictionless eigenfrequency of the lagoon. This allowed us to study the effect of resonance in the lagoon. We performed simulations to obtain values for $\sigma/\sigma_0 = 0$ up to $\sigma/\sigma_0 = 2$, with a step size of 0.02, to investigate the effects of a sub-critical lagoon ($\sigma/\sigma_0 < 1$) as well as a super-critical lagoon ($\sigma/\sigma_0 > 1$). Furthermore, we multiplied a friction coefficient with a correction factor to investigate the influence of friction. We used a correction factor for an inlet channel (1) with default friction, (2) with 10% of the default friction, (3) with 1% of the default friction and (4) with no friction.

1.4.3 Apply the model to the Adriatic Sea and compare the results with complex model simulations (RQ3)

As a final step, we tested our idealized model, by comparing a simulation of the Adriatic Sea that included the Venice lagoon and the Marano-Grado lagoon, with the results of a complex model (Ferrarin et al., 2017). Parameters such as the geometry of the Adriatic Sea, are taken from literature and Google Earth. We transform the basic model into a more realistic Adriatic Sea model in four steps. First, we split the sea basin into five compartments with different depths. Second, we consider a lagoon with multiple inlet channels. Third, we consider 2 lagoons with location and dimensions that are based on the Venice lagoon and the Marano-Grado lagoon. Fourth, we consider a Dirichlet boundary condition at the open boundary of the sea basin. Then, we compared the final model with the aforementioned complex model of the Adriatic Sea. We compared the amphidromic systems of the M_2 tidal constituent and the K_1 tidal constituent. Specifically, we studied the tidal range of the sea basin, the tidal range difference between simulations with lagoons and simulations without lagoons, the shift of the amphidromic point for the M_2 tidal constituent and the volume transport through the inlet channels. By this way, we aimed to establish whether the idealized model is suitable in giving a realistic representation of the tidal interaction between a lagoon and the adjacent sea.

1.5 Report outline

This report is organized as follows. Section 2 presents the idealized model. In section 3, the results of the parameter sensitivity analysis and the application to the Adriatic Sea, are presented. Section 4 and section 5 contain the discussion and the conclusion of the study, respectively.

2 Model

2.1 Model formulation

Consider a number of *lagoons*, connected to a much larger rectangular, semi-enclosed, *sea* basin, with longitudinal coordinate x and lateral coordinate y , sketched in figure 2. The sea basin has a uniform width B and length L . The longitudinal closed boundaries are located at $y = 0$ and $y = B$. A lateral closed boundary is located at $x = 0$, for all values of y , except for the location of an inlet channel: $y \in [y_{\text{ign},i}^{\ominus}, y_{\text{ign},i}^{\oplus}]$. The superscript \ominus denotes the lower y -value of an inlet channel and the superscript \oplus denotes the upper y -value of an inlet channel. The system is forced through an open lateral boundary at $x = L$. The basin may consist of multiple compartments ($j = 1, 2, \dots, J$), each of uniform depth, where the first compartment ($j = 1$) contains the closed boundary and the last compartment ($j = J$) contains the open boundary. The compartments are separated by longitudinal topographic steps at $x = s_j$. Connected to the closed end of the sea basin is a lagoon, with surface area a_{ign} where $a_{\text{ign}} \ll BL$. The basin is connected to a sea through I channels with length ℓ_i , uniform depth h_i and uniform width b_i .

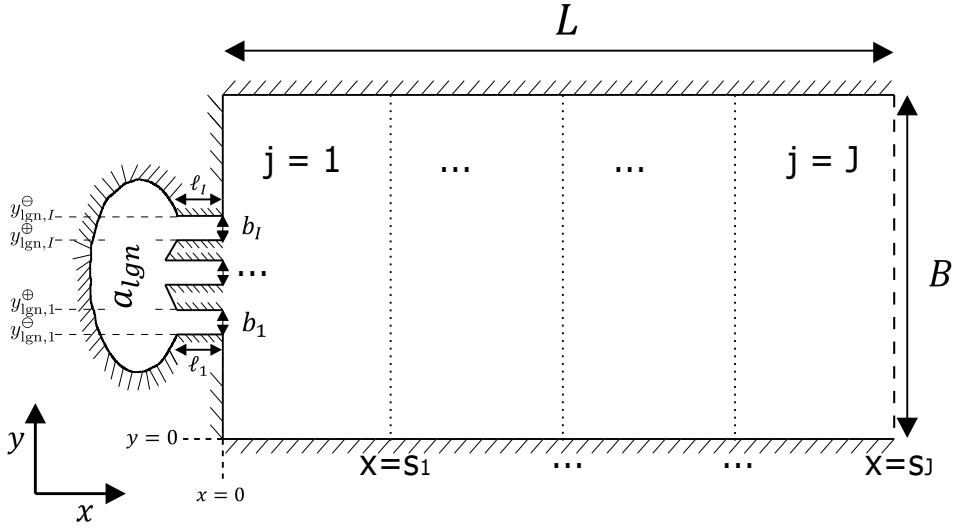


Figure 2: Top view of basin geometry showing one lagoon connected to the sea basin. Dotted lateral lines inside the sea basin represent topographic steps for depth variations. The dashed line at the right-hand side represents the open boundary.

To consider the hydrodynamics of the system, we combine two models: a model for the sea basin and model for the lagoon. First, we apply a two-dimensional, depth-averaged (2DH) model for the sea basin. The linear depth-averaged shallow water equations including bottom friction are represented as follows:

$$\frac{\partial \zeta_j}{\partial t} + H_j \left[\frac{\partial u_j}{\partial x} + \frac{\partial v_j}{\partial y} \right] = 0, \quad (2.1)$$

$$\frac{\partial u_j}{\partial t} - f v_j + \frac{r_j u_j}{H_j} = -g \frac{\partial \zeta_j}{\partial x}, \quad (2.2)$$

$$\frac{\partial v_j}{\partial t} + f u_j + \frac{r_j v_j}{H_j} = -g \frac{\partial \zeta_j}{\partial y}. \quad (2.3)$$

Here, t is time, u_j and v_j denote the depth-averaged flow velocity in the x and y direction, respectively, and ζ_j the free surface elevation with respect to still water level. The subscript j refers to the corresponding compartment (figure 2). Furthermore, $g = 9.8 \text{ m/s}^2$ is the gravitational acceleration, H_j represents the depth of each compartment of the sea, $f = 2\Omega \sin(\phi)$ is a Coriolis parameter where $\Omega = 7.292 \times 10^{-5} \text{ s}^{-1}$ is the angular frequency of Earth's rotation and ϕ is the latitude. A scaling procedure justifying equation (2.1) - (2.3) is provided in Appendix A.1. Moreover, a linear friction

coefficient, obtained from Lorentz' linearisation of a quadratic friction law is introduced (Zimmerman, 1982):

$$r_j = \frac{8c_D U_{\text{sea},j}}{3\pi}, \quad (2.4)$$

with drag coefficient $c_D = 2.5 \times 10^{-3}$ and typical velocity scale $U_{\text{sea},j}$. An iterative procedure to determine the typical velocity scale $U_{\text{sea},j}$ is presented in section 2.3. At the longitudinal boundaries of the model we impose no-normal flow:

$$v_j = 0, \text{ at } y = 0 \text{ and } y = B. \quad (2.5)$$

At the closed boundary of the sea basin, we impose no-normal flow at any position where no inlet channels are present:

$$u_1 = 0, \text{ at } x = 0, y \notin [y_{\text{lgn},i}^{\ominus}, y_{\text{lgn},i}^{\oplus}]. \quad (2.6)$$

At the boundaries across the topographic steps we impose continuity in mass and free surface elevation:

$$u_j H_j = u_{j+1} H_{j+1}, \text{ at } x = s_j, \quad (2.7)$$

$$\zeta_j = \zeta_{j+1}, \text{ at } x = s_j. \quad (2.8)$$

At the open end of the sea basin, we impose a Riemann boundary condition, as a Kelvin wave with coastal amplitude Z_{sea} .

Next, we consider the lagoon as a Helmholtz basin. The flow velocity of a channel $u_{\text{inl},i}$, is assumed to be uniform over length l and width b . Conservation of mass and momentum for these scalar quantities are expressed in the following equations:

$$a_{\text{lgn}} \frac{\partial \zeta_{\text{lgn}}}{\partial t} = \sum_{i=1}^I h_i b_i u_{\text{inl},i}, \quad (2.9)$$

$$\frac{\partial u_{\text{inl},i}}{\partial t} + \frac{r_i u_{\text{inl},i}}{h_i} = -g \frac{\zeta_{\text{lgn}} - \langle \zeta_{\text{sea},i} \rangle}{\ell_i}, \text{ for } i = 1, 2, \dots, I, \quad (2.10)$$

where $\zeta_{\text{sea},i}$ is the free surface elevation at sea at $x = 0, y \in [y_{\text{lgn},i}^{\ominus}, y_{\text{lgn},i}^{\oplus}]$. Similar to the sea basin, a linear coefficient r_i is obtained from Lorentz' linearisation of a quadratic friction law (Zimmerman, 1982):

$$r_i = \frac{8c_D U_{\text{inl},i}}{3\pi}. \quad (2.11)$$

The boundary between the inlet channel and the sea requires continuity in mass transport:

$$\langle u_{\text{sea},i} \rangle H_1 b_i = u_{\text{inl},i} h_i b_i, \text{ for } i = 1, 2, \dots, I. \quad (2.12)$$

We substitute equation (2.10) in the time derivative of equation (2.9) to reduce the set of equations to a single partial differential equation for ζ_{lgn} :

$$\frac{\partial^2 \zeta_{\text{lgn}}}{\partial t^2} = \frac{g}{a_{\text{lgn}}} \sum_{i=1}^I \left[\frac{h_i b_i}{\ell_i} (\langle \zeta_{\text{sea},i} \rangle - \zeta_{\text{lgn}}) \right]. \quad (2.13)$$

where $r_i = 0$. In equation (2.13) we can identify the frictionless eigenfrequency σ_0 of the system:

$$\sigma_0^2 = \frac{g}{a_{\text{lgn}}} \sum_{i=1}^I \frac{h_i b_i}{\ell_i}. \quad (2.14)$$

2.2 Solution method

Consider $\eta_j = (\zeta_j, u_j, v_j)$ as the state in compartment j . We seek a time-periodic solution for equation (2.1) - (2.3) in each compartment in the form of:

$$\eta_j(x, y, t) = \Re\{\hat{\eta}_j(x, y) \exp[-i\sigma t]\}, \quad (2.15)$$

where the complex quantity $\hat{\eta}_j(x, y) = (\hat{\zeta}_j, \hat{u}_j, \hat{v}_j)$ denotes the structure of the wave. Taylor (1922) solved $\hat{\eta}_j(x, y)$ by proposing a superposition of two Kelvin waves and an infinite number of Poincaré modes. We extend this solution for multiple compartments as done by Roos & Schuttelaars (2011).

First, we rewrite equation (2.1) - (2.3) in terms of ζ (Klein-Gordon equation), u and v (polarisation equations) only. A detailed procedure to derive these equations is presented in Appendix A.2. Next, we impose boundary condition (2.6) to find the wavenumbers in each compartment:

$$k_{j,0} = \pm \sqrt{\frac{\sigma^2 \gamma_j}{g H_j}}, \quad (2.16)$$

$$k_{j,n} = \pm \sqrt{\frac{\sigma^2 \gamma_j^2 - f^2}{g H_j \gamma_j} - \frac{n^2 \pi^2}{B^2}} \text{ with } n = 1, 2, \dots, \quad (2.17)$$

where $\gamma_j = 1 + ir_j \sigma^{-1} H_j^{-1}$. A detailed procedure to derive equation (2.16) and (2.17) is presented in Appendix A.3.

In equation (2.16) and (2.17) we can distinguish different types of waves. Firstly, we have an incoming and a reflected *Kelvin Wave*, with wavenumber $k_{j,0}^\ominus$ and $k_{j,0}^\oplus$, respectively. Secondly, we have an infinite number of incoming and reflected Poincaré waves, with wavenumber $k_{j,n}^\ominus$ and $k_{j,n}^\oplus$, respectively. We substitute the wavenumber $k_{j,0}$ in the general solution for the problem, to find an expression for $\tilde{\eta}_{j,0}^\oplus(y) = (\hat{\zeta}_{j,0}^\oplus, \hat{u}_{j,0}^\oplus, \hat{v}_{j,0}^\oplus)$ and $\tilde{\eta}_{j,0}^\ominus(y) = (\hat{\zeta}_{j,0}^\ominus, \hat{u}_{j,0}^\ominus, \hat{v}_{j,0}^\ominus)$. This gives us the following expressions for the Kelvin waves:

$$\hat{\zeta}_{j,0}^\oplus = a_{j,0}^\oplus \exp\left[\frac{-y}{R_j \sqrt{\gamma_j}}\right], \quad \hat{u}_{j,0}^\oplus = a_{j,0}^\oplus \sqrt{\frac{g}{H_j}} \exp\left[\frac{-y}{R_j \sqrt{\gamma_j}}\right], \quad \hat{v}_{j,0}^\oplus = 0, \quad (2.18)$$

$$\hat{\zeta}_{j,0}^\ominus = a_{j,0}^\ominus \exp\left[\frac{-(B-y)}{R_j \sqrt{\gamma_j}}\right], \quad \hat{u}_{j,0}^\ominus = -a_{j,0}^\ominus \sqrt{\frac{g}{H_j}} \exp\left[\frac{-(B-y)}{R_j \sqrt{\gamma_j}}\right], \quad \hat{v}_{j,0}^\ominus = 0, \quad (2.19)$$

where the *Rossby deformation radius* $R_j = \sqrt{\frac{g H_j}{f}}$ is an e-folding length scale that characterises the decay of the surface elevation amplitude from the coast in the offshore direction and the coefficient $a_{j,0}$ denotes the elevation amplitude at the coast $y = B$ for the incoming Kelvin wave and $y = 0$ for the reflected Kelvin wave. For the Poincaré modes, we apply the same procedure with wavenumber $k_{j,n}$ to find an expression for $\tilde{\eta}_{j,n}^\oplus(y) = (\hat{\zeta}_{j,n}^\oplus, \hat{u}_{j,n}^\oplus, \hat{v}_{j,n}^\oplus)$ and $\tilde{\eta}_{j,n}^\ominus(y) = (\hat{\zeta}_{j,n}^\ominus, \hat{u}_{j,n}^\ominus, \hat{v}_{j,n}^\ominus)$:

$$\hat{\zeta}_{j,n} = a_n \left[\cos(\beta_n y) - \frac{f k_{j,n}}{\beta_n \gamma_j \sigma} \sin(\beta_n y) \right], \quad \text{with } \beta = \frac{n\pi}{B}, \quad (2.20)$$

$$\hat{u}_{j,n} = a_n \sqrt{\frac{g}{H_j \gamma_j^2}} \left[\sqrt{\frac{g}{H_j}} \frac{k_{j,n}}{\sigma} \cos(\beta_n y) - \frac{f}{\beta_n \sqrt{\frac{g}{H_j}}} \sin(\beta_n y) \right], \quad (2.21)$$

$$\hat{v}_{j,n} = i a_n \sqrt{\frac{g}{H_j \gamma_j^2}} \left[\frac{\beta_n^2 \frac{g}{H_j} + f^2 \gamma_j}{\beta_n \gamma_j \sigma \frac{g}{H_j}} \sin(\beta_n y) \right], \quad (2.22)$$

with $k_{j,n} = k_{j,n}^\oplus$ and $a_n = a_n^\oplus$ for the incoming Poincaré waves and $k_{j,n} = k_{j,n}^\ominus$ and $a_n = a_n^\ominus$ for the reflected Poincaré waves. Finally, we compute the superposition of two Kelvin waves and a finite number of Poincaré modes:

$$\hat{\eta}(x, y) = \sum_{m=0}^M [\tilde{\eta}_{j,m}^\oplus(y) \exp(-ik_{j,m}^\oplus[x - s_{j-1}]) + \tilde{\eta}_{j,m}^\ominus(y) \exp(-ik_{j,m}^\ominus[x - s_j])], \quad (2.23)$$

for $j = 1, \dots, J - 1$, where $m = 0$ represents the Kelvin wave, and M is the so-called truncation number that characterises the highest Poincaré mode. In compartment J , we impose the Riemann boundary condition as an incoming Kelvin wave, meaning no Poincaré modes are bound to the open end. Therefore, the solution in compartment J writes:

$$\hat{\eta}(x, y) = \sum_{m=0}^M [\tilde{\eta}_{j,m}^{\oplus}(y) \exp(-ik_{j,m}^{\oplus}[x - s_{j-1}])] + Z_{\text{sea}} \tilde{\eta}_{j,0}^{\ominus}(y) \exp(-ik_{j,0}^{\ominus}[x - L]), \quad (2.24)$$

where the second term characterises the Riemann boundary condition.

For the scalar quantities of the lagoons, we seek a time-periodic solution in the form of:

$$\zeta_{\text{lgn}}(t) = \Re \left\{ \hat{\zeta}_{\text{lgn}} \exp(-i\sigma t) \right\}, \quad (2.25)$$

$$u_{\text{inl},i}(t) = \Re \left\{ \hat{u}_{\text{inl},i} \exp(-i\sigma t) \right\}, \quad (2.26)$$

where $\hat{\zeta}_{\text{lgn}}$ is the free surface elevation amplitude inside the Helmholtz basin and $\hat{u}_{\text{inl},i}$ is the current velocity amplitude in an inlet channel. By substituting equation (2.25) and (2.26) in the mass and momentum balance in equation (2.9) and equation (2.10), we get the following linear system:

$$-i\sigma a_{\text{lgn}} \hat{\zeta}_{\text{lgn}} - \sum_{i=1}^I h_i b_i \hat{u}_{\text{inl},i} = 0, \quad (2.27)$$

$$\frac{g}{\ell_i} \hat{\zeta}_{\text{lgn}} - i\sigma \gamma_{\text{inl},i} \hat{u}_{\text{inl},i} = \frac{g}{\ell_i} \langle \hat{\zeta}_{\text{sea},i} \rangle, \text{ for } i = 1, 2, \dots, I. \quad (2.28)$$

To find the solution of the system, we need to solve the coefficients $a_{j,n}^{\oplus}$ and $a_{j,n}^{\ominus}$ as well as the scalar quantities of the Helmholtz basin $\hat{\zeta}_{\text{lgn}}$ and $\hat{u}_{\text{inl},i}$. We impose boundary condition (2.6) - (2.8) to solve $a_{j,n}^{\oplus}$ and $a_{j,n}^{\ominus}$. We impose boundary condition (2.12) to couple the two systems and solve $\hat{\zeta}_{\text{lgn}}$ and $\hat{u}_{\text{inl},i}$. This leads to a linear system, which we can solve using standard matrix operations. A detailed description of how this linear system is set up, is presented in Appendix B.

2.3 Procedure to determine the bottom friction coefficient

We use an iterative procedure to compute the bottom friction coefficient for each compartment in the basin (r_j) and in the inlet channels of the lagoon (r_i). To calculate the friction coefficient with equation (2.4) and (2.11) for the sea and the lagoon, respectively, we require typical velocity scales:

$$U_{\text{sea},j} = \sqrt{\frac{1}{BL_j} \int_0^B \int_{s_{j-1}}^{s_j} |\hat{u}_j|^2 + |\hat{v}_j|^2 dx dy}, \quad (2.29)$$

$$U_{\text{inl},i} = |\hat{u}_{\text{inl},i}|. \quad (2.30)$$

For the first iteration, we compute an initial velocity scale:

$$U_{\text{sea},j} = Z_{\text{sea}} \sqrt{\frac{g}{H_j}},$$

$$U_{\text{inl},i} = \sqrt{\frac{g}{h_i}}.$$

After every iteration, we update the friction coefficient according to equation (2.29) and (2.30) for the sea basin and the lagoon, respectively. The difference between the new velocity scale and the previous velocity scale is subjected to a threshold value. This threshold value states that we allow a maximum difference of 1 cm/s in the inlet channels and 0.1 cm/s in the sea basin. These threshold values are chosen such that the difference is no more than roughly 1%, based on the average current velocity in the Adriatic Sea, which is in the order of 10 cm/s in the inlet channels and the order of 1 cm/s in the sea basin (Ferrarin et al., 2017). The iteration procedure is repeated until the computed typical velocity scale deviates no more from the previous simulation than our prescribed threshold values.

To investigate the relative influence of friction in the inlet channel of the lagoon, we introduce an artificial dimensionless coefficient p_{fric} :

$$r_{\text{eff},i} = p_{\text{fric}} r_i, \quad (2.31)$$

where the default value of p_{fric} is 1. We apply equation (2.31) after the above described iterative procedure is completed. Note that we only apply equation (2.31) for the basic model in section 3.1. In the Adriatic Sea model, p_{fric} is always set to the default value of 1.

3 Results

We perform simulations with two types of models: the basic model and the Adriatic Sea model. The basic model, illustrated in figure 3a, is discussed in section 3.1 and the Adriatic Sea model, illustrated in figure 3b, is discussed in section 3.2. Important dimensions and parameters of the models are presented in table 1.

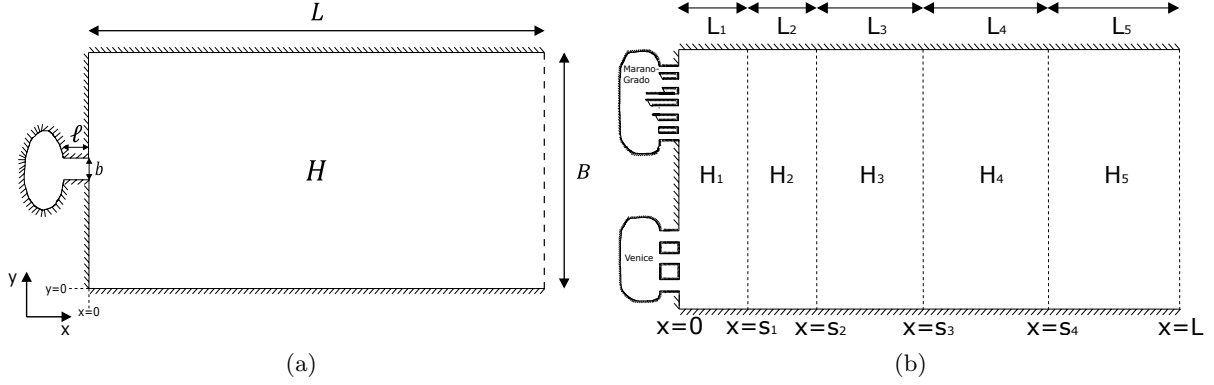


Figure 3: Top view of the geometry of (a) the basic model and (b) the Adriatic Sea model. Dimensions and other relevant parameters are displayed in table 1.

Table 1: Dimensions and (dynamic) parameters of the models. Parameters of the Adriatic Sea are taken from The European Marine Observation and Data Network (2019); Roos & Schuttelaars (2011); Ferrarin et al. (2017). Data of lagoons is taken from Umgiesser et al. (2004); Ferrarin & Umgiesser (2005); Ferrarin et al. (2015, 2017) and Google Earth.

<i>symbol</i>	<i>Input parameters sea basin</i>	<i>Basic model</i>	<i>Adriatic Sea</i>	<i>Unit</i>	
φ	Latitude	43	43	$^{\circ}\text{N}$	
B	Basin width	141	141	km	
L	Basin length	760	760	km	
J	Number of compartments	1	5	[-]	
L_j	Compartment length	760	30, 70, 180, 220, 260	km	
h	Water depth op compartments	150	10, 20, 40, 150, 600	m	
σ	tidal frequency	1.4	\mathbf{M}_2 : 1.4 \mathbf{K}_1 : 0.7	$\times 10^{-4} \text{ s}^{-1}$ $\times 10^{-4} \text{ s}^{-1}$	
Z_{sea}	Boundary condition amplitude	0.1	\mathbf{M}_2 : 0.07 \mathbf{K}_1 : 0.05	m m	
<i>Dynamic parameters sea basin</i>					
R	Rossby deformation radius	385	100, 141, 199, 385, 771	km	
c_0	Phase-speed of Kelvin wave	38	10, 14, 20, 38, 77	m/s	
$ \Im\{k_1\} ^{-1}$	Poincaré decay length	32	\mathbf{M}_2 : 50, 47, 46, 45, 45 \mathbf{K}_1 : 43, 44, 44, 45, 45	km km	
λ_0	Kelvin wavelength	1710	\mathbf{M}_2 : 440, 620, 890, 1710 3430 \mathbf{K}_1 : 840, 1200, 1700 3300, 6600	km km	
<i>Lagoon parameter</i>			<i>Venice lagoon</i>	<i>Marano-Grado lagoon</i>	
y_{IGN}	Location inlet channels	70.5	10, 22, 34	127, 118, 113, 108, 103, 100	km
ℓ	Length inlet channels	2.0	2.5, 2.5, 2.5	1.1, 0.7, 2.4, 1.8, 1.3, 1.3	km
b	Width inlet channels	900	550, 500, 1000	158, 326, 278, 363, 237, 300	m
h	Depth inlet channels	15	10, 16, 8	8, 8, 8, 8, 8, 8	m
a_{IGN}	Surface area	0.0 - 13400	415	160	km ²
σ/σ_0	Dimensionless tidal frequency	0 - 2	\mathbf{M}_2 : 0.3 \mathbf{K}_1 : 0.2	\mathbf{M}_2 : 0.2 \mathbf{K}_1 : 0.1	[-] [-]

3.1 Interaction lagoon and adjacent sea

This section presents how lagoons affect the tidal dynamics of the sea by considering the position of the amphidromic point. We found that the presence of a sub-critical lagoon causes an along-basin shift in the amphidromic point *towards* the lagoon (figure 4a and b). On the contrary, the presence of a super-critical lagoon causes an along-basin shift *away* from the lagoon (figure 4c and d). When the lagoon is close to frictionless resonance, the along-basin shifts of the amphidromic point magnify significantly (figure 4b and c). Cross-basin shifts of the amphidromic point do not occur in the absence of friction in the basic model. Figure 5 illustrates that in the presence of friction, both along-basin shifts and cross-basin shifts of the amphidromic point occur. Analogous to the frictionless case, sub-critical lagoons cause an along-basin shift in amphidromic point towards the lagoon, while super-critical lagoons cause an along-basin shift in amphidromic point away from the lagoon. The magnitude of the shifts is damped due to the effects of bottom friction. Cross-basin shifts occur only towards the reflected Kelvin wave and are in the same order of magnitude as the along-basin shifts in the presence of friction. The most significant cross-basin shifts occur when the lagoon is close to frictionless resonance. In the following subsections, we investigate the tidal dynamics of the lagoon and radiation damping further, to unravel why these along-basin and cross-basin shifts in the amphidromic point occur.

3.1.1 Along-basin shifts of amphidromic point

To investigate the along-basin shift of the amphidromic point, we consider the effect of radiation damping. We define a *radiating wave* and compare it with the Kelvin waves. We will consider only the Kelvin modes of the waves because although Poincaré modes are important to simulate the tidal dynamics of the basin, they do not contribute to our understanding of the along-basin shift of the amphidromic point. The surface elevation of the radiating wave is computed according to:

$$\hat{\zeta}_{\text{rad},0}(x, y) = \hat{\zeta}_0^\oplus(x, y) - \hat{\zeta}_{\text{ref},0}^\oplus(x, y), \quad (3.1)$$

where $\hat{\zeta}_{\text{rad},0}^\oplus(x, y)$ is the surface elevation of the radiating wave, $\hat{\zeta}_0^\oplus(x, y)$ is the surface elevation of the reflected Kelvin wave and $\hat{\zeta}_{\text{ref},0}^\oplus(x, y)$ is the surface elevation of the reflected Kelvin wave in a sea basin without the influence of a lagoon. Furthermore, we calculate the phase-lag of the radiating wave with respect to the reflected Kelvin wave:

$$\Delta\phi_{\text{rad}} = \arg \left[\frac{\hat{\zeta}_{\text{rad},0}}{\hat{\zeta}_{\text{ref},0}^\oplus} \right] \text{ at } x = 0, y = y_{\text{lgn},1}^{\text{mid}}, \quad (3.2)$$

where $y_{\text{lgn},1}^{\text{mid}}$ is positioned in the middle of the inlet channel. Moreover, we calculate the phase-lag of the free surface elevation inside the lagoon with respect to the free surface elevation just outside the inlet channel:

$$\Delta\phi_{\text{lgn}} = \arg \left[\frac{\hat{\zeta}_{\text{lgn}}}{\hat{\zeta}_{\text{sea}}} \right] \text{ at } x = 0, y = y_{\text{lgn},1}^{\text{mid}}. \quad (3.3)$$

We use equation (3.2) and (3.3) to analyse the phase of the radiating wave and the lagoon, respectively, in section 3.1.1.1 and 3.1.1.2.

3.1.1.1 Frictionless interaction

To understand how lagoons affect the tidal dynamics, first, we investigate the phase of the tide inside the lagoon, second the phase and the amplitude of the radiating wave, and third the along-basin shift of the amphidromic point.

First, we investigate the phase of the tide inside the lagoon, which also governs the volume transport through the inlet channel. In the absence of friction, the volume transport lags the phase of the tide inside the lagoon 90° . Figure 6a illustrates that for a sub-critical lagoon, the tide inside the lagoon is in phase with the tide outside the inlet channel. On the contrary, for a super-critical lagoon, the tide inside the lagoon lags the phase of the tide outside the inlet channel by 180° . This means that the volume transport of a sub-critical lagoon is directed towards the lagoon during the rising tide and

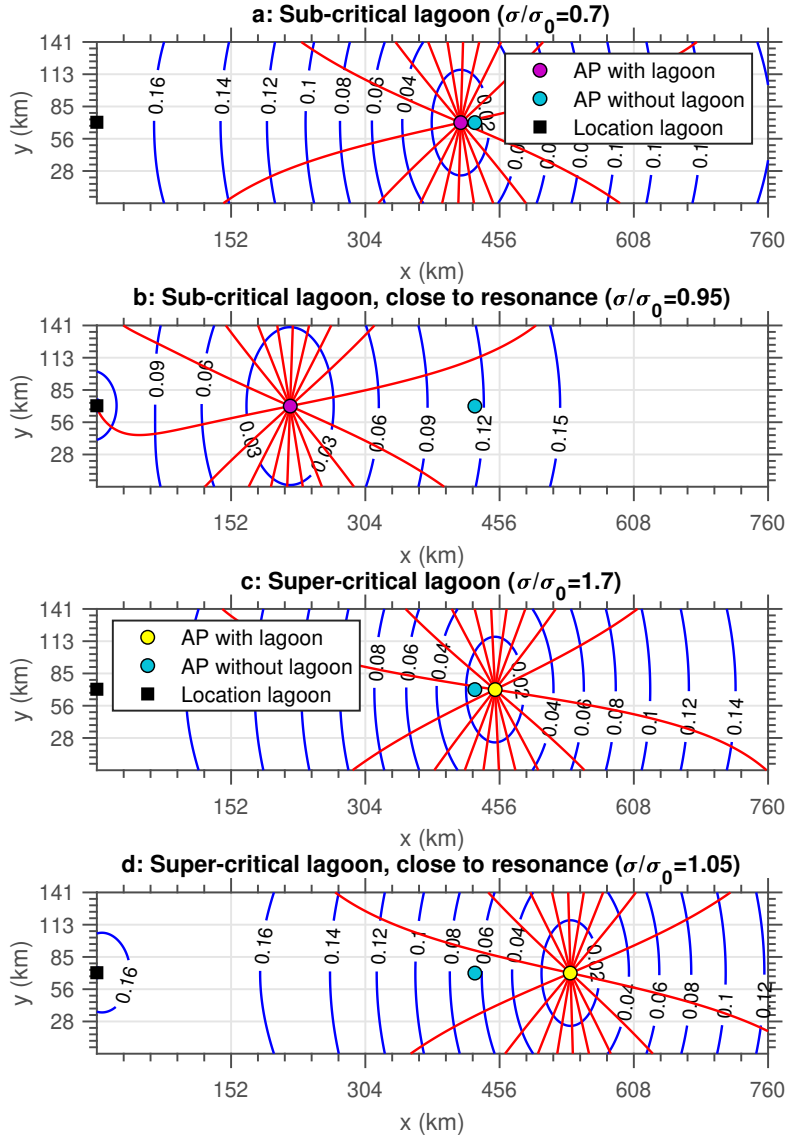


Figure 4: Amphidromic system for M_2 tidal constituent of the *frictionless* basin, (a and b) with a sub-critical lagoon and (c and d) with a super-critical lagoon. Co-range contours (in blue) are in 2 cm intervals. Co-phase lines (in red), for a tidal period of 12.42 hours, are in 18 intervals.

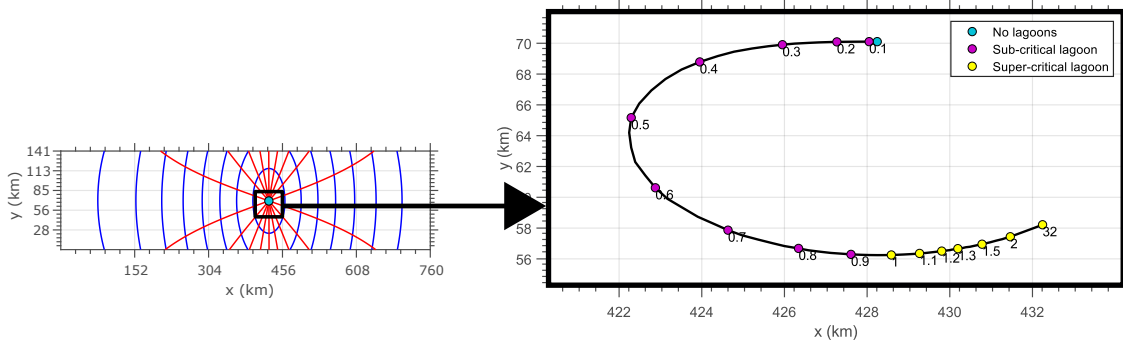


Figure 5: (left) Amphidromic system of a basin including friction and (right) a close zoom of the basin, illustrating the shift of the amphidromic point due to a lagoon. p_{fric} is set to the default value of 1. Position of the amphidromic point of the basin is displayed for σ/σ_0 ranging from 0.1 to 32. The effects due to sub-critical lagoons are denoted with a purple dot, and the effects due to super-critical lagoons are denoted with a yellow dot. The black line through the dots represents the position of the amphidromic point for intermediate values of σ/σ_0 .

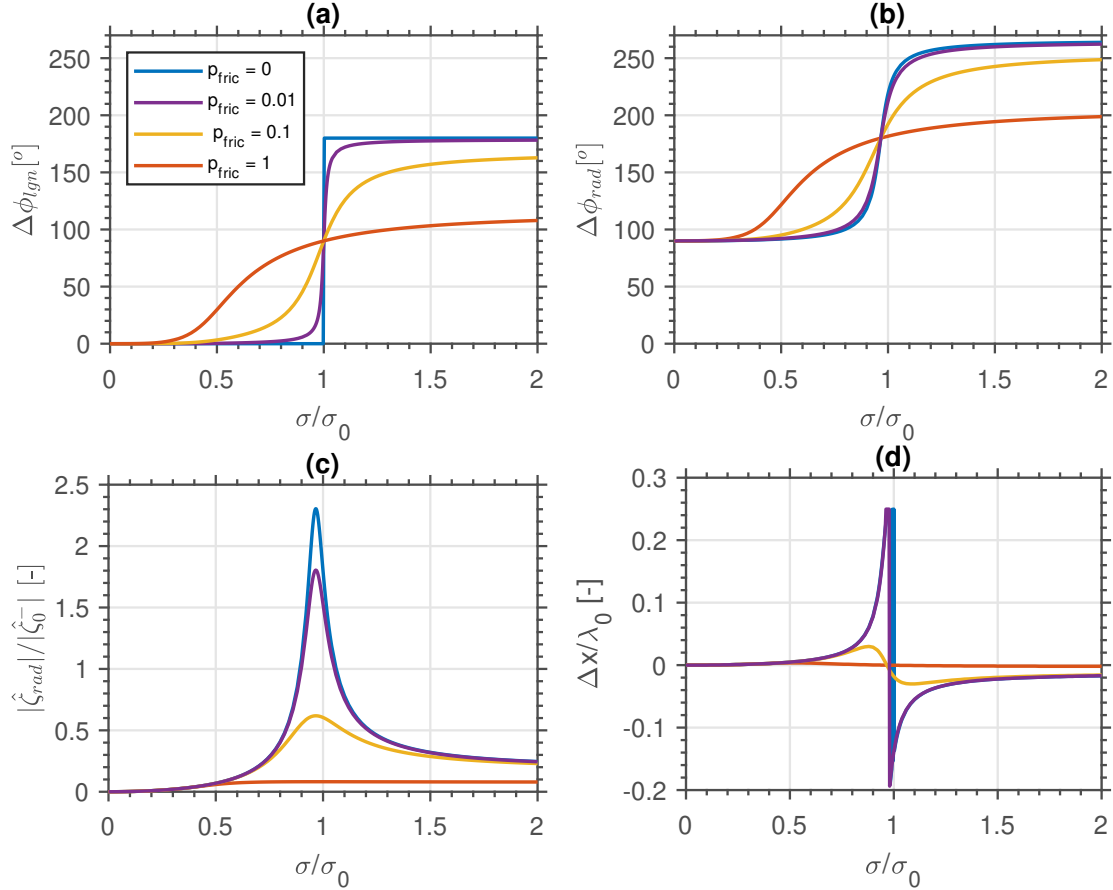


Figure 6: Model results of the basic model illustrating (a) the phase-lag between surface elevation inside the lagoon and the surface elevation just outside the lagoon, (b) the phase-lag between the radiating wave and the reflected Kelvin wave, just outside the inlet channel, (c) the elevation amplitude of the radiating wave, normalized by amplitude of the incoming Kelvin wave and (d) the along-basin (x) shift of the amphidromic point. Positive values in (d) indicate a shift towards the lagoon and negative values indicate a shift away from the lagoon.

the volume transport of a super-critical lagoon is directed towards the sea during the rising tide. The volume transport through the inlet channel is entirely due to the radiating wave (Roos & Schuttelaars, 2015). Therefore, this mechanism is essential to understand the dynamics of the radiating wave.

Next, we study the phase-lag and the amplitude of the radiating wave to understand how the sea is affected by the lagoon. Figure 6b illustrates that the radiating wave *lags* the reflected Kelvin wave 90° to 180° for a sub-critical lagoon. This induces a lag in the phase of the reflected Kelvin wave. For a super-critical lagoon, the radiating wave *leads* the reflected Kelvin wave 90° to 180° . This induces a boost in the phase of the reflected Kelvin wave. The magnitude of the lag or boost in the phase of the reflected Kelvin wave depends on the elevation amplitude of the radiating wave. Figure 6c illustrates that the elevation amplitude of the radiating wave amplifies exponentially towards $\sigma/\sigma_0 = 1$, increasing the effects on the reflected Kelvin wave.

As a final step, we study the shift in the amphidromic point to unravel how the lagoon affects the tidal dynamics of the sea. Figure 6d illustrates that the radiating wave causes the amphidromic point to shift towards a sub-critical lagoon, and away from a super-critical lagoon. When the surface elevation amplitude of the radiating wave amplifies close to $\sigma/\sigma_0 = 1$ (figure 6c), the shift of the amphidromic point magnifies significantly as well.

3.1.1.2 The effects of friction

Bottom friction damps the effects of the lagoon on the tidal dynamics of the sea. Figure 6a illustrates that when bottom friction is included, the phase-lag of the tide inside the lagoon shows a smooth transition from 0° to 180° , instead of a sudden shift at $\sigma/\sigma_0 = 1$. Furthermore, a smoother transition in the phase-lag between the radiating wave and the reflected Kelvin wave is shown in figure 6b. As energy dissipates in the inlet channels due to bottom friction, the amplitude of the radiating wave in figure 6c is suppressed for increasing values of p_{fric} . This reduces the shift in the amphidromic point in figure 6d, compared to the frictionless system.

3.1.2 Cross-basin shifts of the amphidromic point

Cross-basin shifts of the amphidromic point occur in the presence of friction. Relatively high current velocities in the inlet channels lead to energy dissipation, which naturally damps the amplitude of the reflected Kelvin wave (figure 7a), leading to a cross-basin shift of the amphidromic point (figure 7b). Besides high current velocities in the inlet channels, the tidal current of the sea just outside the inlet channels is enhanced as well, contributing to the amplitude loss of the reflected Kelvin wave.

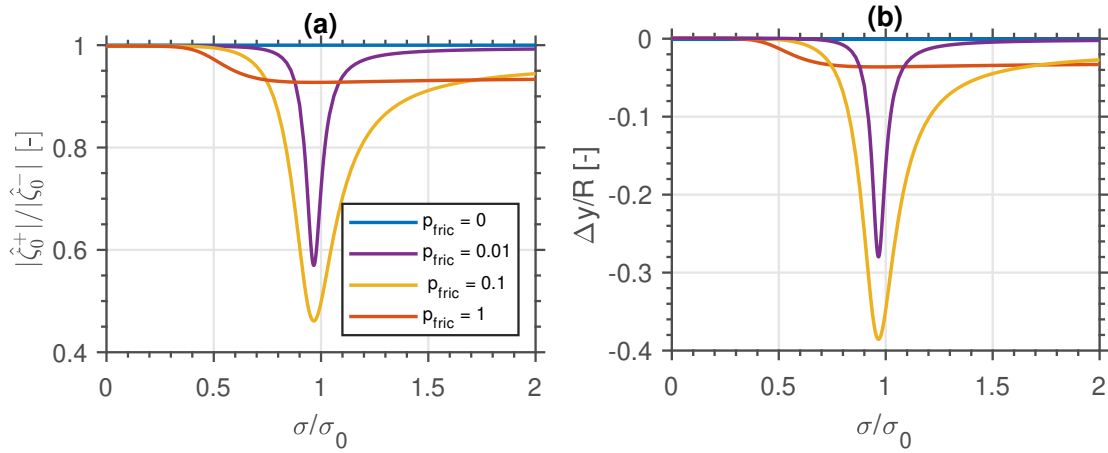


Figure 7: (a) The amplitude loss of the reflected Kelvin wave with respect to the incoming Kelvin wave and (b) the cross-basin shift of the amphidromic point, normalized by the Rossby deformation radius.

3.2 Application to the Adriatic Sea and comparison with complex model simulations

In this section, our idealized model is tested against the results of the *complex model* of Ferrarin et al. (2017). We transform the basic model into a more realistic Adriatic Sea model in four steps. First, we split the sea basin into five compartments with different depths. Second, we consider a lagoon with multiple inlet channels. Third, we consider 2 lagoons with location and dimensions that are based on the Venice lagoon and the Marano-Grado lagoon. Fourth, we impose a Dirichlet boundary condition (instead of Riemann boundary condition) at the open boundary of the sea basin. We present a more detailed methodology and intermediate results of every step in Appendix C. In this section, we will only consider the model we obtained after the fourth step.

We simulated the tidal dynamics of the M_2 and the K_1 tidal constituent of the Adriatic Sea. Dimensions and other important parameters for this model are displayed in table 1. We investigate the correspondence between the complex model and the idealized model with four indicators: (1) the tidal range in the sea basin, (2) the tidal range difference between simulations with lagoons and simulations without lagoons, (3) the shift of the amphidromic point for the M_2 tidal constituent and, (4) the volume transport through the inlet channels.

To illustrate the quantitative difference between the tidal range of the idealized model and the complex model, we express the differences as a fraction of the maximum tidal range in the complex model:

$$DIFF = \frac{|\hat{\zeta}|_{\text{idealized}} - |\hat{\zeta}|_{\text{complex}}}{\max(|\hat{\zeta}|_{\text{complex}})} \times 100\%. \quad (3.4)$$

To compute the tidal range difference and the volume transport through the inlet channels we apply a similar approach as Ferrarin et al. (2017). To calculate the tidal range difference we subtract the tidal range of the scenario without lagoons from the scenario that includes lagoons. Furthermore, we determine the average volume transport through the inlet channels with the following equation:

$$Q(t) = \Re \left\{ \sum_{i=1}^I b_i h_i [\hat{u}_{i,M_2} \exp(-i\sigma_{M_2} t) + \hat{u}_{i,S_2} \exp(-i\sigma_{S_2} t) + \hat{u}_{i,K_1} \exp(-i\sigma_{K_1} t)] \right\}. \quad (3.5)$$

To compute the average volume transport through the inlet channels, we take the average of $|Q(t)|$ over 12 months.

The results of the idealized model show good correspondence with the results of the complex model, as shown by the four aforementioned indicators. Firstly, the M_2 tidal range (figure 8) of the idealized model, shows a similar pattern as the surface elevation of the complex model. Numerical values diverge up to $DIFF = 4\%$ in the basin, with the exception of the closed end of the basin, where values diverge up to $DIFF = 37\%$. Similarly to the M_2 tidal range, the K_1 tidal range (figure 9) of the idealized model shows a similar pattern as the complex model and numerical values diverge no more than $DIFF = 11\%$ anywhere in the basin. Secondly, for the elevation amplitude differences of the M_2 and K_1 tidal constituent, we found that our results show good agreement with the results of the complex model, illustrated in figure 10 and 11, respectively. The amplitude difference of the M_2 tidal constituent, is a straightforward result from the shift in the amphidromic point, as illustrated in figure 10. However, close to the Venice lagoon, the surface elevation amplifies significantly. This increase in the surface elevation amplitude is a result of hydrostatic pressure in the lagoon. The amplification of the surface elevation inside the lagoon generates a pressure gradient that extends for several kilometres in the sea basin, away from the lagoon. Thirdly, the shift of the amphidromic point is 9.2 km North-West in the idealized model in contrast to 10 km North-West in the complex model. Fourthly, the volume transport through the inlet channels, displayed in table 2, shows almost identical results for the Marano-Grado lagoon. The total flux of the Venice lagoon is overestimated by 10%.

Table 2: The average volume transport $|Q(t)|$ through the inlet channels over 12 months of the M_2 , S_2 and K_1 tidal constituent computed by a complex model (Ferrarin et al., 2017) and an idealized model of the Adriatic Sea. The *total transport* denotes the sum of the volume transport through all the inlet channels of the lagoon. The *range* denotes the range of the volume transport in the individual inlet channels.

Lagoon	Complex model		Idealized model	
	<i>Total transport</i>	<i>Range</i>	<i>Total transport</i>	<i>Range</i>
Venice	7800 m ³ /s	1900 - 3100 m ³ /s	8600 m ³ /s	2000 - 3500 m ³ /s
Marano-Grado	3400 m ³ /s	60 - 1100 m ³ /s	3400 m ³ /s	300 - 1100 m ³ /s

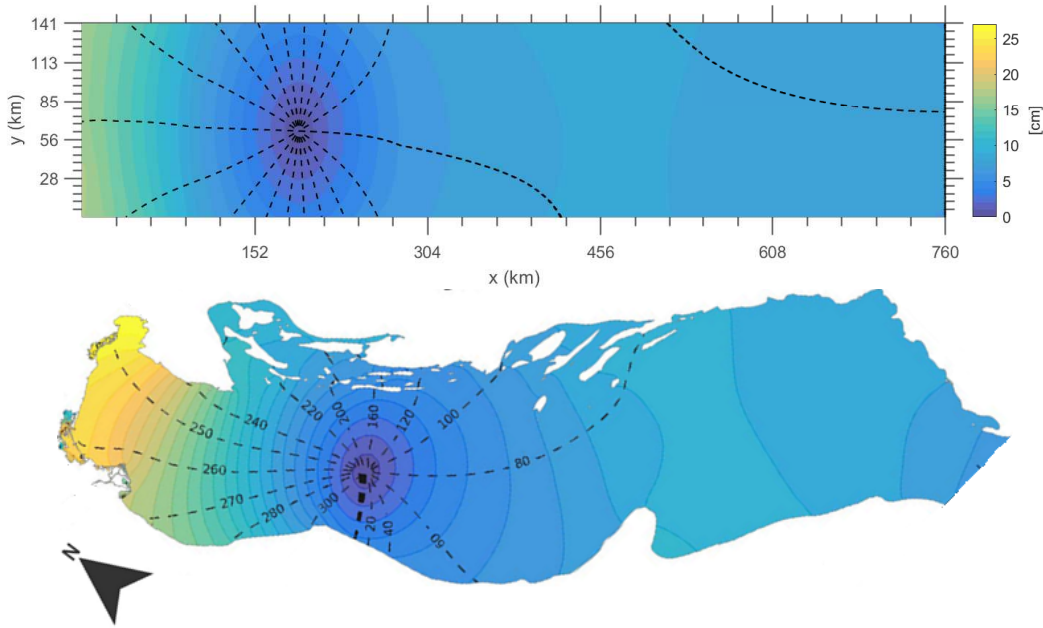


Figure 8: M_2 amplitude and phase computed from the simulation of (above) the idealized model and (below) the complex model of Ferrarin et al. (2017). Colour scale is identical for both figures.

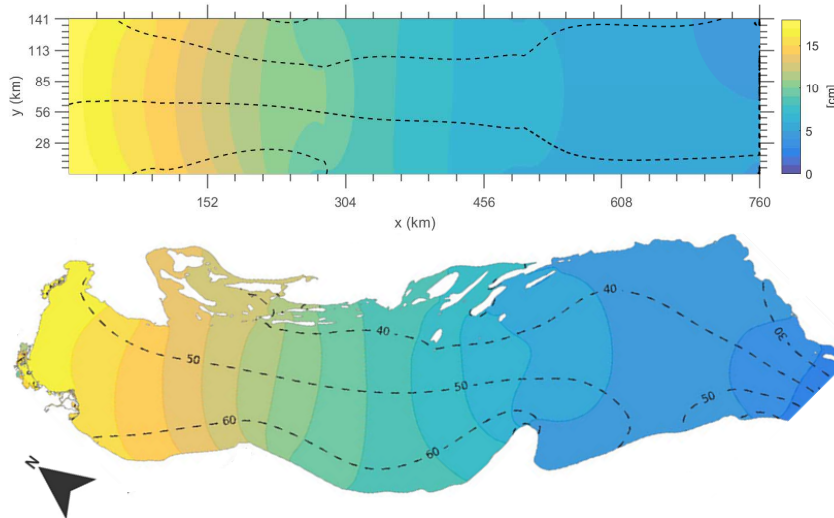


Figure 9: K_1 amplitude and phase computed from the simulation of (above) the idealized model and (below) the complex model of Ferrarin et al. (2017). Colour scale is identical for both figures.

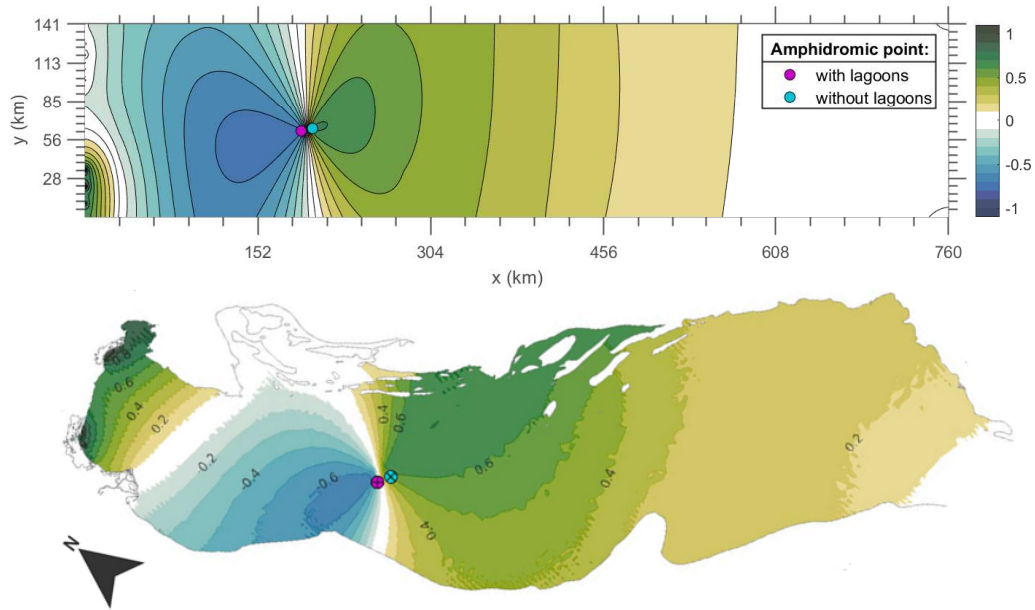


Figure 10: M_2 amplitude difference between simulation with lagoons and simulation without lagoons of (above) the idealized model and (below) the complex model of Ferrarin et al. (2017). Amplitude difference is computed as the results of the simulation that includes lagoons minus the reference simulation without lagoons. Colour scale is identical for both figures.

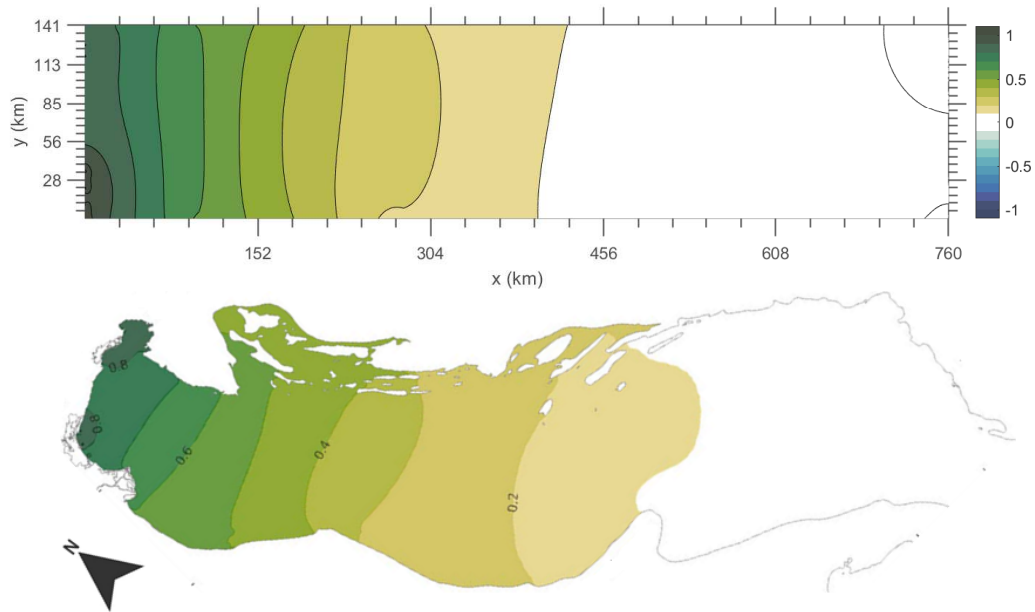


Figure 11: K_1 amplitude difference between simulation with lagoons and simulation without lagoons of (above) the idealized model and (below) the complex model of Ferrarin et al. (2017). Amplitude difference is computed as the results of the simulation that includes lagoons minus the reference simulation without lagoons. Colour scale is identical for both figures.

4 Discussion

4.1 Along-basin shift of the amphidromic point

In this study, we investigated how lagoons affect the large-scale tidal dynamics of the sea. The results show that a radiating wave is induced by the lagoon, leading to a shift of the amphidromic point. To unravel why the effects of the radiating wave lead to a shift in the amphidromic point, we will analyse the response of a 1-D model without the effects of friction and Coriolis. Consider a one-dimensional semi-infinite channel, forced through an incoming wave, with a Helmholtz basin at the closed end of the channel, illustrated in figure 12.

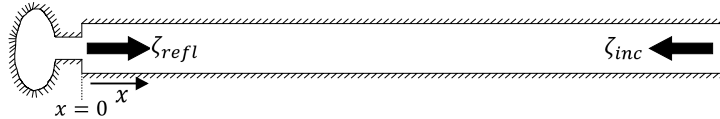


Figure 12: Top view of a 1D basin geometry, with a Helmholtz basin connected at the closed end. The arrows denote the direction of propagation of the incoming wave and the reflected wave.

We write the solution for the surface elevation as the superposition of an incoming wave and a reflected wave:

$$\zeta(x, t) = \zeta_{inc} \cos(kx + \sigma t) + \zeta_{refl} \cos(kx - \sigma t - \Phi), \quad (4.1)$$

where all quantities are real-valued and Φ is the phase-lag due to the radiating wave. Assuming that in the absence of friction no amplitude loss occurs, we can rewrite the equation using trigonometric identities to the following form:

$$\frac{\zeta(x, t)}{\zeta_{refl}} = 2 \cos(kx - \frac{1}{2}\Phi) \cos(\sigma t + \frac{1}{2}\Phi). \quad (4.2)$$

The term $\cos(kx - \frac{1}{2}\Phi)$ denotes the horizontal structure of the amphidromic system. If $\Phi < 0$, the amphidromic system shifts to the negative x -direction and if $\Phi > 0$, the amphidromic system shifts to the positive x -direction. Our model results have shown that a sub-critical lagoon indeed implies that $\Phi < 0$ and a super-critical lagoon implies that $\Phi > 0$. Therefore, we conclude that the shift of the amphidromic point is a result of the phase-lag of the reflected wave, caused by the radiating wave.

The above-discussed 1-D model shows us that the radiating wave, induced by the lagoon, naturally leads to an along-basin shift of the amphidromic system. Previous research has already shown that the solution for the shallow water equations in a tidal basin can be found by the superposition of an incoming wave, a reflected wave and a radiating wave (Miles, 1971). Additionally, Roos & Schuttelaars (2015) showed that the presence of Helmholtz basins may significantly affect the tidal response outside the basin. Furthermore, they found that the way a Helmholtz basin influences the tidal response depends on whether the basin is sub-critical or super-critical. Our results indeed confirm that the effects of a Helmholtz basin depend on whether the basin is sub-critical or super-critical. Additionally, we showed that the radiating wave originating from the inlet channel affects the tidal phase of the adjacent sea and thus lead to along-basin shifts in the amphidromic system.

4.2 Cross-basin shift of the amphidromic point

Besides an along-basin shift of the amphidromic system, the Helmholtz basin also induces a cross-basin shift of the amphidromic point. A cross-basin shift of the amphidromic point occurs only in the presence of friction in our model. Hendershott & Speranza (1971) suggested that cross-basin shifts of the amphidromic point occur due to energy dissipation. Although we did not quantify the energy fluxes in the model, the amplitude-loss of the reflected Kelvin wave shows that energy dissipation is responsible for the cross-basin shift of the amphidromic point. Previous studies have already shown that bottom friction (Rienecker & Teubner, 1980), as well as viscous effects (Roos & Schuttelaars, 2011) in the sea basin, lead to energy dissipation.

To put the significance of the cross-basin shift of the amphidromic point induced by the lagoons in our Adriatic Sea model in a broader perspective, we compare the frictional effects of the lagoon to the frictional effects of the sea basin. First, we consider the cross-basin position of the amphidromic point with- and without friction, when lagoons are excluded in our Adriatic Sea model. Next, we compare this to the effects induced by lagoons, to unravel the relative importance of lagoons. When friction is excluded, the amphidromic point is located symmetrically at $y = 70.5$ km. When friction is included, the amphidromic point shifts 5.4 km in the negative y -direction. The presence of lagoons leads to an additional cross-basin shift of the amphidromic point of 1.8 km in the negative y -direction. Because the frictional effects due to the presence of lagoons are in the same order of magnitude as the large-scale frictional effects of the Adriatic Sea tidal dynamics, we conclude that lagoons are an important aspect of modelling studies to capture the effects of energy dissipation in tidal dynamics.

4.3 Influence of geometry and boundary conditions on the model results

Transforming the basic model into a more realistic Adriatic Sea model with a step-by-step approach gave us some insight into how variations in the lagoon and the sea affect our results. The inclusion of topographic steps in the sea to account for depth variations and a Dirichlet boundary condition at the open boundary to account for the presence of the Mediterranean Sea improves the performance of the model over the sea basin. It does however not affect the direction of the along-basin and cross-basin shift of the amphidromic point due to the presence of the lagoons. The number of inlet channels and the dimensions of the inlet channels affects the tidal current velocity and the tidal range just outside the inlet channels. Enhanced energy dissipation due to high current velocities may overestimate the magnitude of the cross-basin shift of the amphidromic point when only a single inlet channel is included. However, it also does not affect the direction of the along-basin and cross-basin shift of the amphidromic point. Similarly, the cross-basin position of the lagoon affects the tidal range and the tidal currents close to the lagoon, but does not induce significant large-scale effects in the adjacent sea. In summary, strong simplifications of the basin- and lagoon geometry in the basic model affect how accurate the tidal range is represented. However, it does not affect the general trends of how sub-critical or super-critical lagoons affect the position of the amphidromic point.

4.4 Comparison between the idealized model and the complex model

Finally, we tested our model by comparing a simulation of the Adriatic Sea with the results of a complex model. The effect of lagoons in the Adriatic Sea in our idealized model shows good agreement with the results of the complex modelling study (Ferrarin et al., 2017). We acknowledge that due to strong simplifications in our geometry, we do not reproduce the tidal dynamics of the Adriatic Sea as well as the complex model. Although it would be possible to calibrate the parameters and dimensions of our Adriatic Sea model, to match observations in the Adriatic Sea, this would defeat the purpose of a computational efficient idealized model. Moreover, the effects of the tidal interaction between the lagoons and the Adriatic sea of our idealized model are indeed accurate, as we have shown by studying four different indicators. Firstly, the tidal range of the idealized model shows good correspondence with the complex model. Numerical values diverge no more than 11% of the maximal tidal range, with the exception of the tidal range of the M_2 tidal range at the closed end of the basin, which deviates up to 37% of the maximal tidal range. Secondly, the tidal range difference between the scenario with lagoons and without lagoons shows good agreement with the complex model. The M_2 and K_1 tidal range difference show the same pattern, and the numerical values are all in the same order of magnitude. Thirdly, the tidal volume transport between each lagoon and the Adriatic Sea match the results of the complex model. This is shown by the small deviations of total volume transport between the two models. The total volume transport for the Venice lagoon deviates 10% from the complex model and the total volume transport of the Marano-Grado lagoon is almost identical to the complex model. Fourthly, the shift of the amphidromic point of the M_2 tidal constituent of our idealized model (9.2 km North West), matches the shift of the amphidromic point of the complex model (10.0 km North West).

Ferrarin et al. (2017) found that the lagoons in de Adriatic Sea significantly influence the entire Adriatic Sea tidal dynamics, and cause a shift of the amphidromic point for the M_2 tidal constituent towards the lagoons. The results of our study not only confirm this phenomenon but also show that this shift occurs due to the sub-critical nature of the lagoons. The geometry of the inlet channel and

the surface area of the lagoon affect the proximity to resonance and thereby the back-effects in the Adriatic Sea. This implies that — as the proximity to resonance of the lagoon governs the response in the adjacent sea — altering the geometry of the lagoons (e.g. through dredging operations) may cause back-effects in the adjacent sea.

5 Conclusion and outlook

In this study, we unravelled how lagoons affect the large-scale tidal dynamics of an adjacent sea, such as the Adriatic Sea. We used an idealized model to study the tidal interaction between a lagoon and a sea. The results showed that a radiating wave originates from the lagoon, causing an along-basin shift of the amphidromic system. Additionally, enhanced energy dissipation due to bottom friction in the inlet channels of the lagoons causes a cross-basin shift of the amphidromic point. In this section, we seek to answer chronologically the research questions formulated in this study:

RQ1. *How can we develop an idealized model to investigate the tidal interaction between a lagoon and an adjacent sea?*

First, we developed an idealized model of the tidal dynamics of a rectangular semi-enclosed sea basin including lagoons. We extended Roos & Schuttelaars' (2011) version of Taylor's (1922) model to account for the presence of Helmholtz basins connected to the closed end. The model proved to be computationally efficient and allowed for an extensive parameter sensitivity analysis, making it a convenient tool to study the tidal interaction between tidal inlet systems and an adjacent sea. Whereas tidal inlet systems such as lagoons, estuaries and wetlands exist in coastal areas all over the world, their role in open-sea tidal dynamics is still poorly investigated. Our model provides a quick analysis tool to unravel the large-scale effects of these basins and to investigate whether external effects such as human intervention or sea-level rise have a significant back-effect.

RQ2. *How do lagoons affect the large-scale tidal dynamics of an adjacent sea?*

Next, we unravelled how lagoons affect the large-scale tidal dynamics of an adjacent sea. Oscillations within the lagoon trigger co-oscillations, radiating waves back into the sea (Maas, 1997). We investigated how the radiating waves affect the reflected Kelvin wave in the absence of friction. We found that the nature of the response depends on whether the lagoon is sub-critical (with an eigenfrequency above the forcing tidal frequency) or super-critical (with an eigenfrequency below the forcing tidal frequency). For a sub-critical lagoon, the tidal surface elevation inside the lagoon is in phase with the tidal surface elevation just outside the inlet channel. Therefore the lagoon attracts water during the rising tide and releases water during the falling tide. This leads to a radiating wave that is scattered into the sea. The radiating wave lags behind the reflected Kelvin wave which causes a shift of the amphidromic system towards the lagoon. For a super-critical lagoon, the tidal surface elevation inside the lagoon lags the tidal surface elevation just outside the inlet channel by 180° . This leads to a radiative wave that leads the reflected Kelvin wave, causing a shift of the amphidromic point away from the lagoon. Frictional effects within the inlet channel damp the surface elevation amplitude of the radiating wave and cause an additional phase-lag with respect to the reflected Kelvin wave. Moreover, the effect of bottom friction leads to energy dissipation in the inlet channels, resulting in a cross-basin shift of the amphidromic point. In summary, we found that lagoons induce a radiating wave that influences the phase of the reflected Kelvin wave, and enhances energy dissipation in the inlet channel. Together this results in along-basin and cross-basin shifts of the amphidromic point.

RQ3. *Can we simulate the effects of lagoons in the Adriatic Sea while maintaining our idealized modeling approach?*

As a final step, we tested our model by comparing a simulation of the Adriatic Sea with the results of a complex model (Ferrarin et al., 2017). Despite simplified geometry and a simplified description of physics, our idealized model showed good agreement with the complex model. For this, it is essential to capture the proximity to resonance of the lagoons accurately. As the proximity to resonance of the lagoon regulates the back-effects in the Adriatic Sea, alterations of the lagoon (e.g. through dredging operations) may cause back-effects in the sea.

Future work may include studying the morphological effects induced by lagoons. The shift of the amphidromic system affects the tidal currents in the basin and therefore influences the sediment transport

in the sea. This may affect the long-term bathymetry of the sea, playing an important role in navigation and dredging operations. Furthermore, morphological stability in the lagoons has an important role in how lagoons affect the adjacent sea on long-term. Unstable equilibria may lead to long-term changes in the geometry of the inlet channels and thereby affect its response at sea. To predict these morphological effects we require a more detailed modelling approach for the lagoons, as the Helmholtz basin does not consider any spatial variation in the lagoon.

The model can be applied for systems with a similar geometry: a sea basin that roughly represents the geometry of a semi-enclosed basin with tidal inlet systems connected to the closed end of the sea. Implementing the model for other basins may put our results in a broader perspective. Furthermore, the model can be extended to account for tidal inlet systems at the closed boundaries at the side of the sea basin, to study how this affects the tidal interaction between the tidal inlet system and the sea.

References

- Brouwer, R. L., Schuttelaars, H. M. & Roos, P. C. (2013). Modelling the influence of spatially varying hydrodynamics on the cross-sectional stability of double inlet systems. *Ocean Dynamics*, *63*(11-12), 1263–1278. doi: 10.1007/s10236-013-0657-6
- Brown, P. J. (1973). Kelvin-wave Reflection in a Semi-infinite Canal. *Sears Foundation for Marine Research*, *31*(1), 153–164.
- Ferrarin, C., Maicu, F. & Umgiesser, G. (2017). The effect of lagoons on Adriatic Sea tidal dynamics. *Ocean Modelling*, *119*, 57–71. doi: 10.1016/j.ocemod.2017.09.009
- Ferrarin, C., Tomasin, A., Bajo, M., Petrizzo, A. & Umgiesser, G. (2015). Tidal changes in a heavily modified coastal wetland. *Continental Shelf Research*, *101*, 22–33. doi: 10.1016/j.csr.2015.04.002
- Ferrarin, C. & Umgiesser, G. (2005). Hydrodynamic modeling of a coastal lagoon: The Cabras lagoon in Sardinia, Italy. *Ecological Modelling*, *188*(2-4), 340–357. doi: 10.1016/j.ecolmodel.2005.01.061
- Garrett, C. (1975). Tides in gulfs. *Deep-Sea Research*, *22*, 23–35.
- Glaeser, J. D. (1978). Global Distribution of Barrier Islands in Terms of Tectonic Setting. *The Journal of Geology*, *86*(3), 283–297.
- Hendershott, M. C. & Speranza, A. (1971). Co-oscillating tides in long, narrow bays; the Taylor problem revisited. *Deep Sea Research and Oceanographic ...*, *18*(10), 959–980. Retrieved from <http://linkinghub.elsevier.com/retrieve/pii/0011747171900027> doi: 10.1016/0011-7471(71)90002-7
- Herman, A. (2007). Numerical modelling of water transport processes in partially-connected tidal basins. *Coastal Engineering*, *54*(4), 297–320. doi: 10.1016/j.coastaleng.2006.10.003
- Kumar, M., Schuttelaars, H. M., Roos, P. C. & Möller, M. (2015). Three-dimensional semi-idealized model for tidal motion in tidal estuaries. *Ocean Dynamics*, *66*(1), 99–118. doi: 10.1007/s10236-015-0903-1
- Maas, L. R. (1997). On the nonlinear Helmholtz response of almost-enclosed tidal basins with sloping bottoms. *Journal of Fluid Mechanics*, *349*, 361–380. doi: 10.1017/S0022112097006824
- Miles, J. (1971). Resonant response of harbours: an equivalent-circuit analysis. *Journal of Fluid Mechanics*, *46*(02), 241. Retrieved from http://www.journals.cambridge.org/abstract_S002211207100051X doi: 10.1017/S002211207100051X
- Miles, J. & Munk, W. (1961). Harbor Paradox. *Journal of the Waterways and Harbors Division*, *87*(3), 111-132.
- Murray, A. B. (2003). Contrasting the goals, strategies, and predictions associated with simplified numerical models and detailed simulations. *Geophysical Monograph Series*, *135*(January 2003), 151–165. doi: 10.1029/135GM11
- Rienecker, M. & Teubner, M. (1980). A note on frictional effects in Taylor’s problem. *J Mar Res*, *2*(38), 1263–1278.
- Roos, P. C. & Schuttelaars, H. M. (2009). Horizontally viscous effects in a tidal basin: Extending Taylor’s problem. *Journal of Fluid Mechanics*, *640*, 421–439. doi: 10.1017/S0022112009991327
- Roos, P. C. & Schuttelaars, H. M. (2011). Influence of topography on tide propagation and amplification in semi-enclosed basins. *Ocean Dynamics*, *61*(1), 21–38. doi: 10.1007/s10236-010-0340-0
- Roos, P. C. & Schuttelaars, H. M. (2015). Resonance properties of tidal channels with multiple retention basins: role of adjacent sea. *Ocean Dynamics*, *65*(3), 311–324. doi: 10.1007/s10236-015-0809-y
- Taylor, G. I. (1922). Tidal Oscillations in Gulfs and Rectangular Basins. *Proceedings of the London Mathematical Society*, *s2-20*(1), 148-181. Retrieved from <https://dx.doi.org/10.1112/plms/s2-20.1.148> doi: 10.1112/plms/s2-20.1.148

- The European Marine Observation and Data Network. (2019). *Bathymetry Viewing and Download service*. <https://portal.emodnet-bathymetry.eu/?menu=19>. (Accessed: 30-10-2019)
- Umgiesser, G., Canu, D. M., Cucco, A. & Solidoro, C. (2004). A finite element model for the Venice Lagoon. Development, set up, calibration and validation. *Journal of Marine Systems*, 51(1-4 SPEC. ISS.), 123–145. doi: 10.1016/j.jmarsys.2004.05.009
- Zimmerman, J. T. F. (1982). On the Lorentz linearization of a quadratically damped forced oscillator. *Physics Letters A*, 89(3), 123–124. doi: 10.1016/0375-9601(82)90871-4

Appendices

A Deriving the model equations of the sea basin

A.1 Linearisation of shallow water equations

The horizontal length scale of tidal waves, is much larger than the vertical length scale, in the tidal basins considered in this study (see e.g. table 1 for reference). Therefore, we assume that hydrostatic pressure conditions, allowing the application of the depth-integrated Navier-Stokes equations. We assume the density of water is constant, and the vertical viscous terms are a linear function of the flow velocity. Furthermore, we neglect horizontal viscous terms. The depth-averaged, non-linear, *shallow water equations* can be written as:

$$\frac{\partial \zeta}{\partial t} + \frac{\partial}{\partial x}[u(H + \zeta)] + \frac{\partial}{\partial y}[v(H + \zeta)] = 0, \quad (\text{A.1})$$

$$\frac{\partial u}{\partial t} + u \frac{\partial u}{\partial x} + v \frac{\partial u}{\partial y} - fv + \frac{ru}{H + \zeta} = -g \frac{\partial \zeta}{\partial x}, \quad (\text{A.2})$$

$$\frac{\partial v}{\partial t} + u \frac{\partial v}{\partial x} + v \frac{\partial v}{\partial y} + fu + \frac{rv}{H + \zeta} = -g \frac{\partial \zeta}{\partial y}. \quad (\text{A.3})$$

To determine the relative importance of the remaining terms, a scaling procedure is applied. Therefore, we formulate the following, dimensionless quantities:

$$t^* = \sigma t, \quad \zeta^* = \zeta/Z, \quad r^* = \frac{r}{H\sigma},$$

$$x^* = \frac{x}{L}, \quad u^* = \frac{u}{U}, \quad f^* = \frac{f}{\sigma},$$

$$y^* = \frac{y}{L}, \quad v^* = \frac{v}{U}, \quad \eta^* = \frac{Z}{H},$$

where Z is a typical tidal range scale and U is a typical velocity scale. Substituting the dimensionless quantities in the shallow water equations, gives us the following expressions:

$$[Z\sigma] \frac{\partial \zeta^*}{\partial t^*} + \left[\frac{HU}{L} \right] \left\{ \frac{\partial}{\partial x^*} \left(u^* \left(1 + \frac{Z\zeta^*}{H} \right) \right) + \frac{\partial}{\partial y^*} \left(v^* \left(1 + \frac{Z\zeta^*}{H} \right) \right) \right\} = 0, \quad (\text{A.4})$$

$$[U\sigma] \frac{\partial u^*}{\partial t^*} + \frac{U^2}{L} \left(u^* \frac{\partial u^*}{\partial x^*} + v^* \frac{\partial u^*}{\partial y^*} \right) - U\sigma f^* v^* + U\sigma \frac{H}{H + \zeta^* Z} r^* u^* = \left[-\frac{gZ}{L} \right] \frac{\partial \zeta^*}{\partial x^*}, \quad (\text{A.5})$$

$$[U\sigma] \frac{\partial v^*}{\partial t^*} + \frac{U^2}{L} \left(u^* \frac{\partial v^*}{\partial x^*} + v^* \frac{\partial v^*}{\partial y^*} \right) + U\sigma f^* u^* + U\sigma \frac{H}{H + \zeta^* Z} r^* v^* = \left[-\frac{gZ}{L} \right] \frac{\partial \zeta^*}{\partial y^*}. \quad (\text{A.6})$$

We assume that there is a balance between the elevation change $\left(\frac{\partial \zeta^*}{\partial t^*} \right)$ and the water flow divergence $\left(\frac{\partial}{\partial x^*} \left(u^* \left(1 + \frac{Z\zeta^*}{H} \right) \right) + \frac{\partial}{\partial y^*} \left(v^* \left(1 + \frac{Z\zeta^*}{H} \right) \right) \right)$ in equation (A.4), and we assume that there is a balance between the acceleration $\left(\frac{\partial u^*}{\partial t^*}, \frac{\partial v^*}{\partial t^*} \right)$ and the pressure gradient $\left(\frac{\partial \zeta^*}{\partial x^*}, \frac{\partial \zeta^*}{\partial y^*} \right)$ in equation (A.5) and (A.6). The dimensional coefficients (between square brackets) then lead to a balance between the characteristic flow velocity U , the spatial dimensions and the angular frequency σ :

$$Z\sigma = \frac{HU}{L}. \quad (\text{A.7})$$

Furthermore, the dimensional coefficients of the acceleration term and the pressure term in equation (A.5) and (A.6) display a similar balance:

$$U\sigma = \frac{gZ}{L}. \quad (\text{A.8})$$

Combining equation (A.7) and (A.8) gives us an expression for the characteristic flow velocity U :

$$U = Z\sqrt{\frac{g}{H}}, \quad (\text{A.9})$$

and

$$L = \frac{\sqrt{gH}}{\sigma}. \quad (\text{A.10})$$

Substituting equation (A.9) and (A.10) in equation (A.4) - (A.6) results in the following dimensionless equations:

$$\frac{\partial \zeta^*}{\partial t^*} + \left[\frac{\partial}{\partial x^*} (u^* (1 + \eta^* \zeta^*)) + \frac{\partial}{\partial y^*} (v^* (1 + \eta^* \zeta^*)) \right] = 0, \quad (\text{A.11})$$

$$\frac{\partial u^*}{\partial t^*} + \eta^* \left[u^* \frac{\partial u^*}{\partial x^*} + v^* \frac{\partial u^*}{\partial y^*} \right] - f^* v^* + r^* \frac{u^*}{1 + \eta^* \zeta^*} = -\frac{\partial \zeta^*}{\partial x^*}, \quad (\text{A.12})$$

$$\frac{\partial v^*}{\partial t^*} + \eta^* \left[u^* \frac{\partial v^*}{\partial x^*} + v^* \frac{\partial v^*}{\partial y^*} \right] + f^* u^* + r^* \frac{v^*}{1 + \eta^* \zeta^*} = -\frac{\partial \zeta^*}{\partial y^*}. \quad (\text{A.13})$$

Now we can evaluate the solution using the dimensionless parameter η^* . Considering the Adriatic Sea basin, a typical depth scale $H = 100 - 1200$ m, and a typical surface elevation amplitude $Z < 1$ m. This means that $\eta^* \ll 1$. Therefore, it is shown we can neglect the non-linear advective terms in equation (A.2) - (A.3), as they have a relatively small influence. The shallow water equations are now reduced to the following form:

$$\frac{\partial \zeta}{\partial t} + H \left[\frac{\partial u}{\partial x} + \frac{\partial v}{\partial y} \right] = 0, \quad (\text{A.14})$$

$$\frac{\partial u}{\partial t} - fv + \frac{ru}{H} = -g \frac{\partial \zeta}{\partial x}, \quad (\text{A.15})$$

$$\frac{\partial v}{\partial t} + fu + \frac{rv}{H} = -g \frac{\partial \zeta}{\partial y}. \quad (\text{A.16})$$

A.2 Klein-Gordon equation and the Polarisation equation

To eliminate ζ from equation (A.14) - (A.16), we take the $\frac{\partial}{\partial x}$ of the second momentum balance in equation (A.16), and subtract it from $\frac{\partial}{\partial y}$ of the first momentum balance in equation (A.15):

$$\frac{\partial}{\partial t} \left[\frac{\partial v}{\partial x} - \frac{\partial u}{\partial y} \right] = -f \left[\frac{\partial v}{\partial y} + \frac{\partial u}{\partial x} \right] + \frac{r}{H} \left[\frac{\partial u}{\partial y} - \frac{\partial v}{\partial x} \right]. \quad (\text{A.17})$$

We define the vorticity $\omega = \left[\frac{\partial v}{\partial x} - \frac{\partial u}{\partial y} \right]$. Subsequently, we substitute the continuity equation (A.14) in equation (A.17):

$$\left[\frac{\partial}{\partial t} + \frac{r}{H} \right] \omega = \frac{f}{H} \frac{\partial \zeta}{\partial t}. \quad (\text{A.18})$$

We take the divergence of the momentum balance:

$$\frac{\partial}{\partial t} \left[\frac{\partial u}{\partial x} + \frac{\partial v}{\partial y} \right] - f \left[\frac{\partial v}{\partial x} - \frac{\partial u}{\partial y} \right] + \frac{r}{H} \left[\frac{\partial u}{\partial x} + \frac{\partial v}{\partial y} \right] + g \left[\frac{\partial^2 \zeta}{\partial x^2} + \frac{\partial^2 \zeta}{\partial y^2} \right] = 0. \quad (\text{A.19})$$

We define operator $\Gamma = \frac{\partial}{\partial t} + \frac{r}{H}$ to obtain:

$$-\Gamma^2 \left[\frac{\partial u}{\partial x} + \frac{\partial v}{\partial y} \right] \frac{1}{H} - \Gamma f \omega + \Gamma \left[\frac{\partial^2 \zeta}{\partial x^2} + \frac{\partial^2 \zeta}{\partial y^2} \right] g = 0. \quad (\text{A.20})$$

Finally, we re-arrange the equation to obtain the Klein-Gordon equation:

$$\Gamma^2 \frac{\partial \zeta}{\partial t} + f^2 \frac{\partial \zeta}{\partial t} - \Gamma \left[\frac{\partial^2 \zeta}{\partial x^2} + \frac{\partial^2 \zeta}{\partial y^2} \right] gH = 0. \quad (\text{A.21})$$

Now we seek an equation in terms of u or v only, known as the polarisation equation. To get the polarisation equation, we apply operator Γ to the momentum balance (A.15) and multiply momentum balance (A.16) with f . We compute the sum of the momentum balances to obtain equation (A.22). The same procedure is applied to obtain the second polarisation equation (A.23).

$$u[\Gamma^2 + f^2] + g \left[\Gamma \frac{\partial \zeta}{\partial x} + f \frac{\partial \zeta}{\partial y} \right] = 0. \quad (\text{A.22})$$

$$v[\Gamma^2 + f^2] + g \left[\Gamma \frac{\partial \zeta}{\partial y} - f \frac{\partial \zeta}{\partial x} \right] = 0. \quad (\text{A.23})$$

A.3 Dispersion relation and wavenumber

We now formulate a trial solution for the model:

$$\zeta(x, y, t) = \hat{\zeta}(y) \exp(i[kx - \sigma t]). \quad (\text{A.24})$$

To derive the wavenumber k of the solution, we impose the no-normal flow boundary condition:

$$v = 0 \text{ at } y = 0 \text{ and } y = B, \quad (\text{A.25})$$

and substitute equation (A.25) in equation (A.23):

$$\Gamma \frac{\partial \zeta}{\partial y} - f \frac{\partial \zeta}{\partial x} = 0. \quad (\text{A.26})$$

To express the boundary condition in terms of $\hat{\zeta}(y)$, we will substitute the trial solution (A.24) in boundary condition (A.26) to get the following balance:

$$\exp(i[kx - \sigma t]) \left\{ \frac{\partial \hat{\zeta}}{\partial y} \left[-\sigma i + \frac{r}{H} \right] - f \hat{\zeta} k i \right\} = 0.$$

We now introduce a factor γ :

$$\gamma = 1 + \frac{ir}{\sigma H},$$

and substitute γ in the balance:

$$\exp(i[kx - \sigma t]) \left\{ -\sigma i \gamma \frac{\partial \hat{\zeta}}{\partial y} - f \hat{\zeta} k i \right\} = 0.$$

Because $\exp(i[kx - \sigma t])$ is a periodic function, it can't be zero for all t . This gives us the following expression:

$$-\sigma i \gamma \frac{\partial \hat{\zeta}}{\partial y} - f \hat{\zeta} k i = 0. \quad (\text{A.27})$$

To find a solution for the model, we will substitute the trial solution (A.24) in the Klein Gordon equation (A.21):

$$i \exp(i[kx - \sigma t]) \left(\hat{\zeta} \sigma^3 \gamma^2 - \hat{\zeta} f^2 \sigma - gH \left[\hat{\zeta} k^2 \sigma \gamma - \frac{\partial^2 \hat{\zeta}}{\partial y^2} \sigma \gamma \right] \right) = 0.$$

We rule out the exponential function, for the same argument used for the previous equation, to get the following balance:

$$\alpha^2 = \frac{\sigma^2 \gamma^2 - f^2}{gH \gamma} - k^2.$$

The general solution for $\hat{\zeta}$ reads:

$$\hat{\zeta} = A \cos(\alpha y) + D \sin(\alpha y).$$

Now we can use Boundary condition (A.27) to solve the system:

$$-\sigma\gamma i\alpha[-A \sin(\alpha y) + D \cos(\alpha y)] - fki[A \cos(\alpha y) + D \sin(\alpha y)] = 0.$$

Substituting the values for y gives:

$$A(\sigma\gamma i\alpha \sin(\alpha B) - fki \cos(\alpha B)) + D(-\sigma\gamma i\alpha \cos(\alpha B) - fki \sin(\alpha B)).$$

To solve the coefficients A and D , we write the equations as a linear matrix system:

$$\begin{bmatrix} -fki & -\sigma\gamma i\alpha \\ \sigma\gamma i\alpha \sin(\alpha B) - fki \cos(\alpha B) & -\sigma\gamma i\alpha \cos(\alpha B) - fki \sin(\alpha B) \end{bmatrix} \begin{bmatrix} A \\ D \end{bmatrix} = \begin{bmatrix} 0 \\ 0 \end{bmatrix}.$$

To obtain a non-trivial solution, the determinant of this system must be zero:

$$-gk\sigma\gamma\alpha f g^2 \cos(\alpha B) + g^2 k^2 \sigma^2 \gamma^2 \sin(\alpha B) - [-\alpha^2 f^2 g^2 \sin(\alpha B) - \alpha f g^2 k \sigma \gamma \cos(\alpha B)] = 0.$$

The cosines rule each other out, therefore we get the following expression:

$$-f^2 k^2 \sin(\alpha B) - \sigma^2 \gamma^2 \alpha^2 \sin(\alpha B) = 0.$$

Re-arranging the expression gives us a dispersion relation:

$$\left(k^2 - \frac{\sigma^2 \gamma}{gH}\right) (f^2 - \sigma^2 \gamma^2) \sin(\alpha B) = 0. \quad (\text{A.28})$$

Equation (A.28) gives us two possible solutions for the *wavenumber* k . The first term gives us two possible solutions for the wavenumber of the *Kelvin modes*:

$$k_{j,0} = \pm \sqrt{\frac{\sigma^2 \gamma}{gH}}. \quad (\text{A.29})$$

The third term gives us an infinite number of solutions for the wavenumber of the Poincaré modes:

$$k_{j,n} = \pm \sqrt{\frac{\sigma^2 \gamma^2 - f^2}{gH\gamma} - \frac{n^2 \pi^2}{B^2}} \text{ with } n = 1, 2, \dots \quad (\text{A.30})$$

B Solving the coefficients of the system

In this section we present the solution method for the model derived in section 2 and Appendix A. We need to solve the coefficients $a_{j,m}$ as well as the scalar quantities of the lagoon: $\zeta_{\text{lg}}^{\text{in}}$ and u_{inl} . Therefore, we set up a linear system, that can be solved using standard techniques in e.g. *matlab*. First, recall the solution for the sea basin proposed in section 2:

$$\hat{\eta}(x, y) = \sum_{m=0}^M [\tilde{\eta}_{j,m}^{\oplus}(y) \exp(-ik_{j,m}^{\oplus}[x - s_{j-1}]) + \tilde{\eta}_{j,m}^{\ominus}(y) \exp(-ik_{j,m}^{\ominus}[x - s_j])], \quad (\text{B.1})$$

for $j = 1, \dots, J$, where $m = 0$ represents the Kelvin wave, M is the so-called truncation number that characterises the highest Poincaré mode and $\hat{\eta}_{j,m} = (\hat{\zeta}_{j,m}, \hat{u}_{j,m}, \hat{v}_{j,m})$. For the Kelvin waves we have an expression for $\hat{\eta}_{j,0}$:

$$\hat{\zeta}_{j,0}^{\oplus} = a_{j,0}^{\oplus} \exp\left[\frac{-y}{R_j \sqrt{\gamma_j}}\right], \quad \hat{u}_{j,0}^{\oplus} = a_{j,0}^{\oplus} \sqrt{\frac{g}{H_j}} \exp\left[\frac{-y}{R_j \sqrt{\gamma_j}}\right], \quad \hat{v}_{j,0}^{\oplus} = 0, \quad (\text{B.2})$$

$$\hat{\zeta}_{j,0}^{\ominus} = a_{j,0}^{\ominus} \exp \left[\frac{-(B-y)}{R_j \sqrt{\gamma_j}} \right], \hat{u}_{j,0}^{\ominus} = -a_{j,0}^{\ominus} \sqrt{\frac{g}{H_j}} \exp \left[\frac{-(B-y)}{R_j \sqrt{\gamma_j}} \right], \hat{v}_{j,0}^{\ominus} = 0, \quad (\text{B.3})$$

and for the Poincaré modes we have an expression for $\hat{\eta}_{j,n}$:

$$\hat{\zeta}_{j,n} = a_n \left[\cos(\beta_n y) - \frac{f k_{j,n}}{\beta_n \gamma_j \sigma} \sin(\beta_n y) \right], \text{ with } \beta_n = \frac{n\pi}{B}, \quad (\text{B.4})$$

$$\hat{u}_{j,n} = a_n \sqrt{\frac{g}{H_j \gamma_j^2}} \left[\sqrt{\frac{g}{H_j}} \frac{k_{j,n}}{\sigma} \cos(\beta_n y) - \frac{f}{\beta_n \sqrt{\frac{g}{H_j}}} \sin(\beta_n y) \right], \quad (\text{B.5})$$

$$\hat{v}_{j,n} = i a_n \sqrt{\frac{g}{H_j \gamma_j^2}} \left[\frac{\beta_n^2 \frac{g}{H_j} + f^2 \gamma_j}{\beta_n \gamma_j \sigma \frac{g}{H_j}} \sin(\beta_n y) \right]. \quad (\text{B.6})$$

For the sake of comprehension, we will consider a lagoon with a single inlet in this appendix. We derived a linear system, with 3 unknowns ($\hat{\zeta}_{\text{lgn}}$, \hat{u}_{inl} and $\hat{\zeta}_{\text{sea}}$):

$$-i\sigma a_{\text{lgn}} \hat{\zeta}_{\text{lgn}} - hb \hat{u}_{\text{inl}} = 0, \quad (\text{B.7})$$

$$\frac{g}{\ell} \hat{\zeta}_{\text{lgn}} - i\sigma \gamma_{\text{inl},i} \hat{u}_{\text{inl},i} = \frac{g}{\ell} \langle \hat{\zeta}_{\text{sea}} \rangle. \quad (\text{B.8})$$

Next, recall the boundary conditions for the sea basin:

$$u_1 = 0, \text{ at } x = 0, y \notin [y_{\text{lgn}}^{\ominus}, y_{\text{lgn}}^{\oplus}], \quad (\text{B.9})$$

$$\zeta_j = \zeta_{j+1}, \text{ at } x = s_j, \quad (\text{B.10})$$

$$u_j H_j = u_{j+1} H_{j+1}, \text{ at } x = s_j, \quad (\text{B.11})$$

$$\zeta = \hat{Z}_{\text{sea}} \cos(\sigma t), \text{ at } x = L. \quad (\text{B.12})$$

Note that we use a Dirichlet boundary condition instead of a Riemann boundary condition in this appendix, in order to draft a linear system that is visually more convenient to interpret. As a final step, we couple the lagoon equations to our sea basin through continuity in mass:

$$\langle u_{\text{sea}} \rangle H_1 b = u_{\text{inl}} hb, \text{ at } y \in [y_{\text{lgn}}^{\ominus}, y_{\text{lgn}}^{\oplus}]. \quad (\text{B.13})$$

We introduce one additional boundary condition, simply stating that the seaward free surface elevation of the lagoon equations (ζ_{sea}) should be equal to the free surface elevation from the Taylor problem:

$$\hat{\zeta}_{\text{Taylor}} = \hat{\zeta}_{\text{sea}}. \quad (\text{B.14})$$

Now we set up the linear system to solve the coefficients $a_{j,m}$ as well as the scalar quantities of the lagoon ζ_{lgn} and u_{inl} . By imposing boundary conditions (B.9) - (B.14) on the system, we find a linear system we can solve using standard techniques. On the next page, we present an example of this linear system for a system with $J = 2$, $I = 1$ and Dirichlet boundary condition. The boundary condition for the corresponding rows in the matrix is displayed in the first column. The horizontal and sloping dots denote the poincaré modes that should be added to complete the system.

$$\begin{aligned}
& \left[\begin{array}{l} \text{(B.9)} \\ \& \\ \text{(B.13)} \end{array} \right] \begin{bmatrix} \hat{u}_1^\oplus(y_1) & \dots \\ \vdots & \\ \hat{u}_1^\oplus(y_{\text{ign}}) & \\ \vdots & \\ \hat{u}_1^\ominus(y_M) & \dots \end{bmatrix} \begin{bmatrix} \hat{u}_1^\ominus(y_1) & \dots \\ \vdots & \\ \hat{u}_1^\ominus(y_{\text{ign}}) & \\ \vdots & \\ \hat{u}_1^\ominus(y_M) & \dots \end{bmatrix} \begin{bmatrix} 0 \\ 0 \\ \vdots \\ -h/H_1 \\ 0 \end{bmatrix} \begin{bmatrix} 0 \\ 0 \\ \vdots \\ 0 \\ 0 \end{bmatrix} \\
& \text{(B.10)} \quad \begin{bmatrix} \zeta_j^\oplus(y_1) & \dots \\ \vdots & \\ \zeta_j^\oplus(y_M) & \dots \end{bmatrix} \begin{bmatrix} \zeta_j^\ominus(y_1) & \dots \\ \vdots & \\ \zeta_j^\ominus(y_M) & \dots \end{bmatrix} \begin{bmatrix} \zeta_{j+1}^\oplus(y_1) & \dots \\ \vdots & \\ \zeta_{j+1}^\oplus(y_M) & \dots \end{bmatrix} \begin{bmatrix} \zeta_{j+1}^\ominus(y_1) & \dots \\ \vdots & \\ \zeta_{j+1}^\ominus(y_M) & \dots \end{bmatrix} \begin{bmatrix} 0 \\ 0 \\ \vdots \\ 0 \\ 0 \end{bmatrix} \\
& \text{(B.11)} \quad \begin{bmatrix} u_j^\oplus H_j^\oplus(y_1) & \\ \dots & \\ u_j^\oplus H_j^\oplus(y_M) & \end{bmatrix} \begin{bmatrix} u_j^\ominus H_j^\ominus(y_1) & \\ \dots & \\ u_j^\ominus H_j^\ominus(y_M) & \end{bmatrix} \begin{bmatrix} u_{j+1}^\oplus H_{j+1}^\oplus(y_1) & \\ \dots & \\ u_{j+1}^\oplus H_{j+1}^\oplus(y_M) & \end{bmatrix} \begin{bmatrix} u_{j+1}^\ominus H_{j+1}^\ominus(y_1) & \\ \dots & \\ u_{j+1}^\ominus H_{j+1}^\ominus(y_M) & \end{bmatrix} \begin{bmatrix} 0 \\ 0 \\ \vdots \\ 0 \\ 0 \end{bmatrix} \\
& \text{(B.12)} \quad \begin{bmatrix} 0 \\ 0 \\ \vdots \\ 0 \\ 0 \end{bmatrix} \begin{bmatrix} 0 \\ 0 \\ \vdots \\ 0 \\ 0 \end{bmatrix} \begin{bmatrix} \zeta_j^\oplus(y_1) & \dots \\ \vdots & \\ \zeta_j^\oplus(y_M) & \dots \end{bmatrix} \begin{bmatrix} \zeta_j^\ominus(y_1) & \dots \\ \vdots & \\ \zeta_j^\ominus(y_M) & \dots \end{bmatrix} \begin{bmatrix} 0 \\ 0 \\ \vdots \\ 0 \\ 0 \end{bmatrix} \\
& \text{(B.7)} \quad \begin{bmatrix} 0 \\ 0 \\ \vdots \\ 0 \\ 0 \end{bmatrix} \begin{bmatrix} 0 \\ 0 \\ \vdots \\ 0 \\ 0 \end{bmatrix} \begin{bmatrix} 0 \\ 0 \\ \vdots \\ 0 \\ 0 \end{bmatrix} \begin{bmatrix} 0 \\ 0 \\ \vdots \\ 0 \\ 0 \end{bmatrix} \begin{bmatrix} 0 \\ 0 \\ \vdots \\ 0 \\ 0 \end{bmatrix} \\
& \text{(B.8)} \quad \begin{bmatrix} 0 \\ 0 \\ \vdots \\ 0 \\ 0 \end{bmatrix} \begin{bmatrix} 0 \\ 0 \\ \vdots \\ 0 \\ 0 \end{bmatrix} \begin{bmatrix} 0 \\ 0 \\ \vdots \\ 0 \\ 0 \end{bmatrix} \begin{bmatrix} 0 \\ 0 \\ \vdots \\ 0 \\ 0 \end{bmatrix} \begin{bmatrix} 0 \\ 0 \\ \vdots \\ 0 \\ 0 \end{bmatrix} \\
& \text{(B.14)} \quad \begin{bmatrix} \zeta_1^\oplus(y_{\text{ign}}) \\ \vdots \\ \zeta_1^\oplus(y_M) \end{bmatrix} \begin{bmatrix} \zeta_1^\ominus(y_{\text{ign}}) \\ \vdots \\ \zeta_1^\ominus(y_M) \end{bmatrix} \begin{bmatrix} 0 \\ 0 \\ \vdots \\ 0 \\ 0 \end{bmatrix} \begin{bmatrix} 0 \\ 0 \\ \vdots \\ 0 \\ 0 \end{bmatrix} \begin{bmatrix} 0 \\ 0 \\ \vdots \\ 0 \\ 0 \end{bmatrix} \\
& \text{(B.15)} \quad \begin{bmatrix} \hat{\zeta}_{\text{ign}} \\ \hat{u}_{\text{inl}} \\ \hat{\zeta}_{\text{sea}} \end{bmatrix} \begin{bmatrix} 0 \\ 0 \\ \vdots \\ 0 \\ 0 \end{bmatrix} \begin{bmatrix} 0 \\ 0 \\ \vdots \\ 0 \\ 0 \end{bmatrix} \begin{bmatrix} 0 \\ 0 \\ \vdots \\ 0 \\ 0 \end{bmatrix} \begin{bmatrix} 0 \\ 0 \\ \vdots \\ 0 \\ 0 \end{bmatrix} \\
& \text{(B.16)} \quad \begin{bmatrix} a_j^\oplus \\ \vdots \\ a_j^\ominus \\ \vdots \\ a_{j+1}^\oplus \\ \vdots \\ a_{j+1}^\ominus \\ \vdots \\ a_{j+1}^\oplus \\ \vdots \\ a_{j+1}^\ominus \end{bmatrix} = \begin{bmatrix} 0 \\ 0 \\ \vdots \\ 0 \\ 0 \\ \vdots \\ 0 \end{bmatrix}
\end{aligned}$$

C Transformation from the basic model to the Adriatic Sea model

We presented 2 models in this study: a basic model and an Adriatic Sea model. We made several modifications to the basic model to obtain the Adriatic Sea model presented in section 3.2. In this section we present these modifications and their implications on the simulation results.

To simulate a realistic model of the Adriatic Sea, we transfer the basic model into the Adriatic Sea model in four steps. First, we split the sea basin into five compartments with different depths. Second, we consider a lagoon with multiple inlet channels. Third, we consider 2 lagoons with location and dimensions that are based on the Venice lagoon and the Marano-Grado lagoon. Fourth, we consider a Dirichlet boundary condition (instead of Riemann boundary) at the open boundary of the sea basin. We present model results for the M_2 tidal constituent for each step to put the results of the basic model in a broader perspective. For every step, we analyse the shift of the amphidromic point in the x - and y -direction, the M_2 tidal amplitude and the M_2 tidal amplitude difference due to the presence of the lagoons. Here we particularly focus on the shift of the amphidromic point because we used the position of the amphidromic point to study the tidal interaction between lagoons and the sea in section 3.1. Similar as in section 3.2, we compare the results with the complex model of Ferrarin et al. (2017) in figure 13.

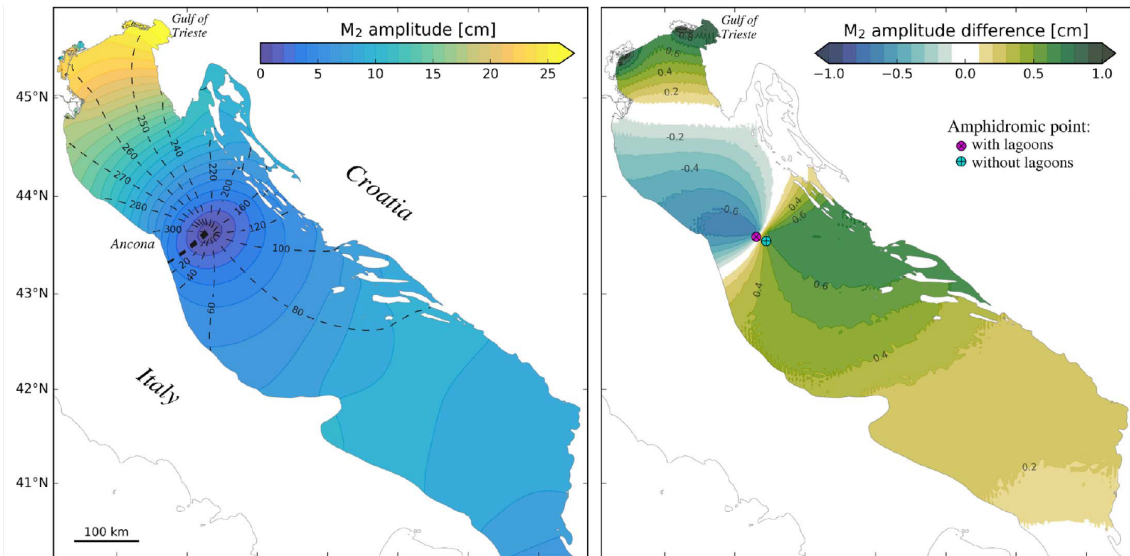


Figure 13: Model results of Ferrarin et al. (2017) for (left) the M_2 tidal range and phase computed from the simulation with the lagoons, and (right) the tidal range difference between the scenario with and without lagoons. Dashed lines (left) denote the co-phase lines. Differences between numerical simulations are computed as the results of the simulation that includes lagoons minus the reference simulation without lagoons. The shift of the amphidromic point is 10 km.

C.1 Basic model

We simulate the basic model with a fixed surface area (see table 3 for relevant parameters). The direction of the cross-basin shift of the amphidromic point (in the negative y -direction) and the along-basin shift of the amphidromic point (in the negative x -direction) in figure 14 is the same as for the complex model. However, numerical values of the tidal range and the tidal range difference diverge significantly between the two models.

Table 3: Parameter values of basic model with a fixed lagoon surface area. Input parameters of the sea basin not shown here are as presented in the third column of table 1 in section 3

<i>symbol</i>	<i>Input parameters sea basin</i>	<i>Unit</i>	
J	Number of compartments	1	[-]
L_j	Compartment length	760	km
h	Water depth op compartments	150	m
$\hat{\zeta}_0^\ominus$	Boundary condition amplitude	0.1	m
<i>Lagoon parameter</i>			
y_{lgn}	Location inlet channels	70.5	km
ℓ	Length inlet channels	2.0	km
b	Width inlet channels	900	m
h	Depth inlet channels	15	m
a_{lgn}	Surface area	536	km ²
σ/σ_0	Dimensionless tidal frequency	0.4	[-]

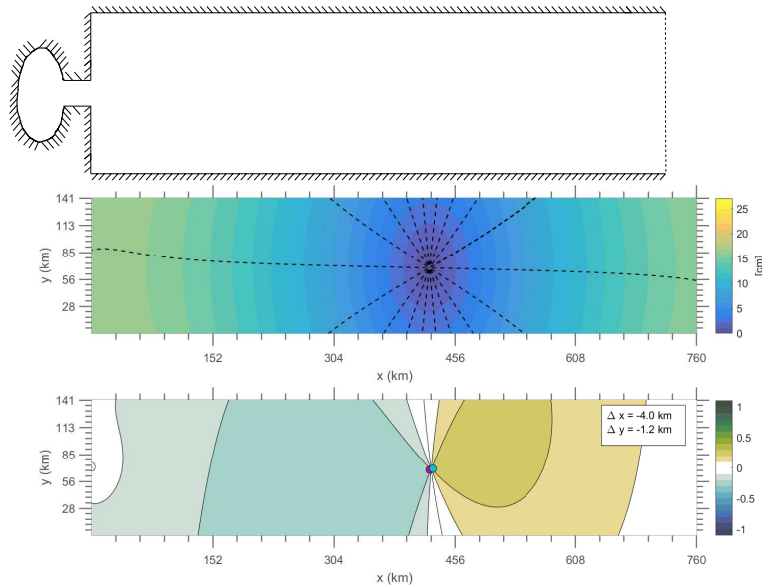


Figure 14: (above) Model geometry, (middle) tidal range, and (below) tidal range difference for the basic model.

C.2 Step 1: Multiple compartments in the sea basin

As a first step, we split the sea basin into five depth compartments to represent a more realistic geometry of the sea basin (see table 3 for relevant parameters). The tidal range (figure 15) has a similar pattern and numerical values as the complex model. The tidal range difference shows some contrast close to the inlet channel, and an increasing contrast towards the open boundary. Again, the direction of the shift of the amphidromic point is the same as in the complex model. While the along-basin shift of the amphidromic point is also similar in numerical values, the cross-basin shift in the idealized model is overestimated compared to the complex model.

Table 4: Parameter values of the extended model with multiple compartments. Input parameters of the sea basin not shown here are as presented in the third column of table 1 in section 3

<i>symbol</i>	<i>Input parameters sea basin</i>		<i>Unit</i>
J	Number of compartments	5	[-]
L_j	Compartment length	30, 70, 180, 220, 260	km
h	Water depth op compartments	10, 20, 40, 150, 600	m
$\hat{\zeta}_0^\ominus$	Boundary condition amplitude	0.055	m
<i>Lagoon parameter</i>			
y_{IGN}	Location inlet channels	70.5	km
ℓ	Length inlet channels	2.0	km
b	Width inlet channels	900	m
h	Depth inlet channels	15	m
a_{IGN}	Surface area	536	km ²
σ/σ_0	Dimensionless tidal frequency	0.4	[-]

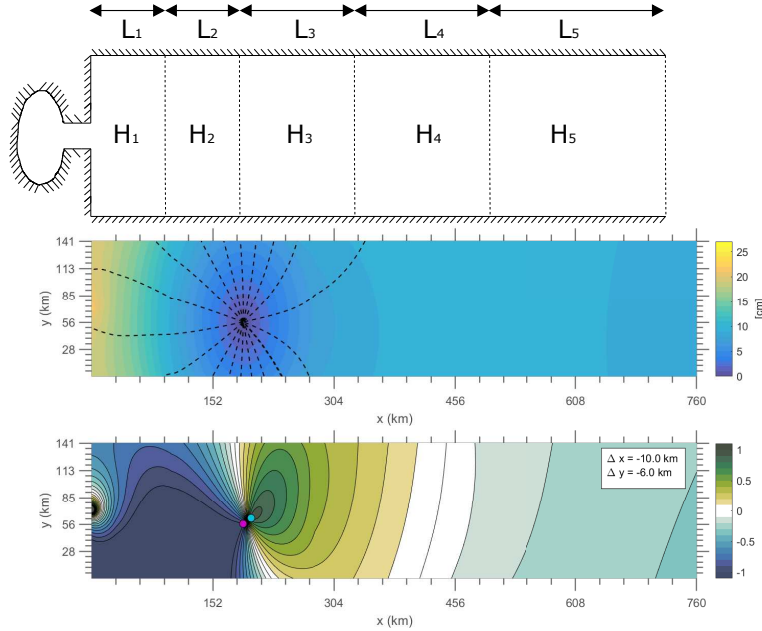


Figure 15: (above) Model geometry, (middle) tidal range, and (below) tidal range difference for the basic model including topographic steps.

C.3 Step 2: Multiple inlet channels in the lagoon

As a second step, the Helmholtz basin is extended with two additional inlet channels to model a more realistic geometry of the lagoon (see table 5 for relevant parameters). Similar as in the previous model, the tidal range difference shows an error at the closed end of the basin and an increasing error close to the open boundary (figure 15). The direction as well as the numerical values of the shift of the amphidromic point Δx and Δy , show good agreement with the complex model.

Table 5: Parameter values of the extended model with multiple inlet channels. Input parameters of the sea basin not shown here are as presented in the third column of table 1 in section 3

<i>symbol</i>	<i>Input parameters sea basin</i>		<i>Unit</i>
J	Number of compartments	5	[-]
L_j	Compartment length	30, 70, 180, 220, 260	km
h	Water depth op compartments	10, 20, 40, 150, 600	m
$\hat{\zeta}_0^\ominus$	Boundary condition amplitude	0.055	m
<i>Lagoon parameter</i>			
y_{IGN}	Location inlet channels	60.5 70.5 80.5	km
ℓ	Length inlet channels	2.0 2.0 2.0	km
b	Width inlet channels	900 900 900	m
h	Depth inlet channels	15 15 15	m
a_{IGN}	Surface area	536	km ²
σ/σ_0	Dimensionless tidal frequency	0.2	[-]

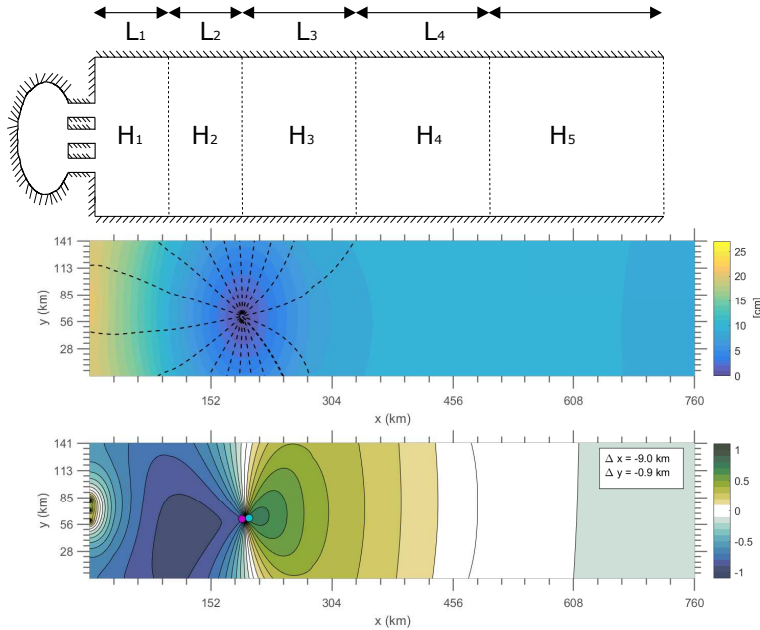


Figure 16: (above) Model geometry, (middle) tidal range, and (below) tidal range difference for the basic model including topographic steps and multiple inlet channels in the lagoon.

C.4 Step 3: Multiple lagoons

As a third step, we extend the model with realistic dimensions and positions for the lagoons (see table 6 for relevant parameters), to represent the Venice lagoon and the Marano-Grado lagoon in a realistic manner. Similar to the previous step, the tidal range shows good agreement (figure 17). Additionally, the tidal range difference at the closed end shows better correspondence with the results of the complex model than in the previous steps. Analogous to the previous step, the tidal range difference shows an increasing error close to the open boundary. The direction as well as the numerical values of the shift of the amphidromic point Δx and Δy , show good agreement with the complex model.

Table 6: Parameter values of the extended model with multiple lagoons with specified locations based on the Venice and Marano-Grado lagoon. Input parameters of the sea basin not shown here are as presented in the third column of table 1 in section 3

<i>symbol</i>	<i>Input parameters sea basin</i>			<i>Unit</i>
J	Number of compartments	5		[-]
L_j	Compartment length	30, 70, 180, 220, 260		km
h	Water depth op compartments	10, 20, 40, 150, 600		m
$\hat{\zeta}_0^\ominus$	Boundary condition amplitude	\mathbf{M}_2 : 0.05		m
<i>Lagoon parameter</i>		<i>Venice lagoon</i>	<i>Marano-Grado lagoon</i>	
y_{ign}	Location inlet channels	10, 22, 34	127, 118, 113, 108, 103, 100	km
ℓ	Length inlet channels	2.5, 2.5, 2.5	1.1, 0.7, 2.4, 1.8, 1.3, 1.3	km
b	Width inlet channels	550, 500, 1000	158, 326, 278, 363, 237, 300	m
h	Depth inlet channels	10, 16, 8	8, 8, 8, 8, 8, 8	m
a_{ign}	Surface area	415	160	km ²
σ/σ_0	Dimensionless tidal frequency	\mathbf{M}_2 : 0.3	\mathbf{M}_2 : 0.2	[-]
		\mathbf{K}_1 : 0.2	\mathbf{K}_1 : 0.1	[-]

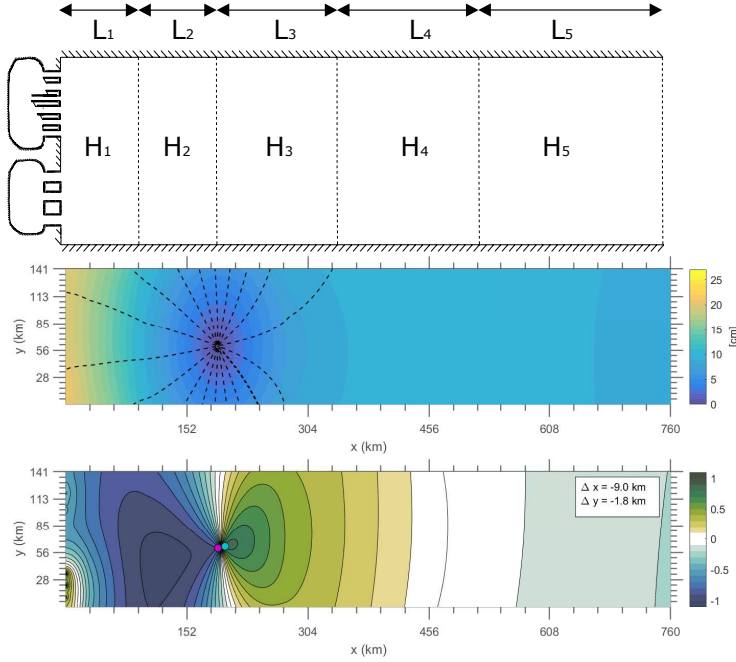


Figure 17: (above) Model geometry, (middle) tidal range, and (below) tidal range difference for the Adriatic Sea model with a Riemann boundary condition.

C.5 Step 4: Dirichlet boundary condition as open boundary

As a final step, we can represent the presence of the Mediterranean Sea more accurately by imposing a Dirichlet boundary condition (a periodic uniform surface elevation at $x = L$). Numerical values for this model are presented in table 1 in section 3. Figure 18 illustrates that, in contrast to the previous steps, the tidal range difference close to the open boundary shows good agreement with the complex model. However, the idealized model underestimates the amplification of the tidal range at the closed end compared to the complex model.

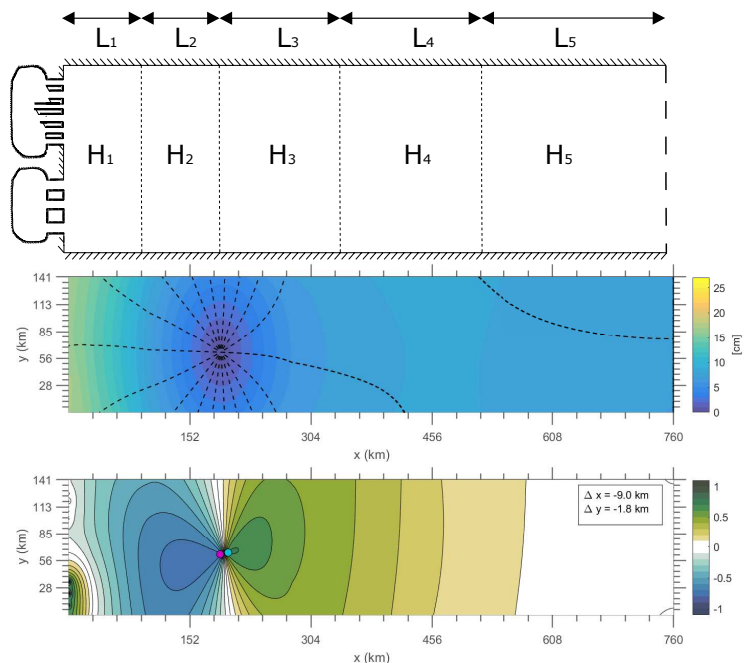


Figure 18: (above) Model geometry, (middle) tidal range, and (below) tidal range difference for the Adriatic Sea model with a Dirichlet boundary condition.